Growth of Thin Films by Pulsed Laser Deposition for Applications in Spin Transport Electronics

by

Adam Hyndman

A thesis submitted in partial
fulfilment of the
requirements for the Degree of
Master of Science
in Physics

University of Canterbury
2009

Abstract

This thesis presents the results of the growth and characterisation of three separate compounds, all of which have been deposited on sapphire, silicon and $SrTiO_3$ substrates using the pulsed laser deposition technique.

The first material studied was cobalt doped titanium dioxide, with initial growths being performed using un-doped TiO_2 targets. These films were used to optimise the growth parameters before introducing $Co:TiO_2$ targets in later growths, where targets with cobalt concentrations of 3, 6 and 12 % were used to grow $Co:TiO_2$ thin films. The $Co:TiO_2$ films were found to be highly oriented, with single phase rutile appearing on the sapphire substrates and single phase anatase being deposited on the $SrTiO_3$ substrates. The films were optically transparent across the visible region, with optical gaps greater than 3 eV. The films showed ferromagnetic behaviour at 10 K and 300 K, with only small reductions in the saturation moments being observed at the higher temperature, indicating the films had a Curie temperature around 600 K.

The second material studied was the half-metallic double perovskite, Sr_2FeMoO_6. In particular the affect of deposition pressure and substrate choice on the structural and magnetic properties of the films was studied. We found the saturation moments of the films to increase dramatically when deposited at 850 ^oC, compared to films deposited at 650 ^oC. The choice of substrate was also

observed to have a large affect on the magnitude of the saturation moments, with films deposited on silicon having the largest observed moments.

Finally a small study was performed on the oxygen deficient $SrFeO_{3-\delta}$, where we managed to grow thin films with varying oxygen concentrations through a combination of altering the oxygen pressure during growth and performing post growth annealing. We found that post growth annealing in oxygen was more effective at introducing oxygen into the films while still maintaining a high crystalline quality.

Acknowledgements

I would like to thank my two supervisors, Prof. Roger Reeves and Dr. Grant Williams for their support and guidance throughout the project.

I would also like to thank the many staff at Industrial Research Limited and faculty members at the University of Canterbury for their willing help in using the various instruments required to produce and analyse thin films. In particular, Dr. John Kennedy for conducting Rutherford backscattering measurements and Harry Jones and Duncan McCann for setting up and performing resistivity measurements.

I acknowledge funding from the New Zealand Foundation for Research, Science and Technology and from the MacDiarmid Institute for Advanced Materials and Nanotechnology.

Last but not least I thank my amazing partner Rose, who kept me on track and spent many hours helping to proof-read this work.

Contents

List of Tables

List of Figures

Chapter 1

Introduction

Current electronic devices are based on the charge of electrons, which are used to transport information through channels in semiconductors, most commonly silicon. Devices based on this technology have enjoyed rapid advancements due to improvements in the fabrication process, allowing smaller channels to be created, which enable smaller, more powerful devices to be made. As these devices continue to reduce in size many believe that they will soon reach a fundamental limit and in order for the electronics industry to continue advancing at its current rate, novel devices will need to be created.

Spin transport electronics, more commonly known as spintronics, is an area of research receiving increasing attention from the scientific community. Spintronics devices propose to utilise the spin of electrons in place, or in conjunction with, electron charge. Electrons are spin ½ fermions, which means they can occupy one of two states of spin, spin-up and spin-down. This spin degree of freedom is currently being used to store information in magnetic mass storage, but has not been utilised in semiconductor technologies because the energy levels of the two spin states are degenerate in commercial semiconductor

materials. While this does pose a problem, recent developments in semiconductor technology are helping to make the spin of electrons resolvable. One of the main advantages over other pioneering technologies, like single electron transistors and molecular-electronics devices, is that spintronics devices are based largely on semiconductors. This means that they will be able to form heterostructures with existing semiconductors, making them easy to integrate into current circuit technologies, which will help to speed up the commercialisation of spintronics based devices.

One of the key elements to making a spintronics device is a spin injector. A successful spin injector must be able to transport a spin polarised current into a non-ferromagnetic material, without degrading the spin current across the interface. While it is relatively simple to make a ferromagnetic metal injector, the degree of spin polarisation is low, at only ~60 %. It is also very difficult to deposit a metal epitaxially on a semiconductor, due to lattice matching problems. Another significant problem is the large difference in conductivities of metals and commercial semiconductor materials, which leads to spin scattering across the interface and therefore a degradation of the spin current. A compelling alternative material for a spin injector is a ferromagnetic semiconductor, they have conductivities on the same order as non-magnetic semiconductors and can be grown epitaxially on top of one another, leading researchers to expect that efficient spin polarised injection will occur across such an interface [1]. The main

obstacle to the commercialisation of such a device, is the lack of a well understood ferromagnetic semiconductor with a Curie temperature above 300 K.

This thesis presents the results of a study on three materials. The dilute magnetic semiconductor, cobalt doped titanium dioxide (Co:TiO_2) that has been shown to be ferromagnetic above room temperature, but is surrounded in controversy due to claims that the ferromagnetism arises from cobalt clustering rather than any intrinsic mechanism [2,3,4]. The half metallic double perovskite, Sr_2FeMoO_6 (SFMO) that has been observed to display a large negative magnetoresistance (MR) [5], exhibit ferrimagnetic behaviour above room temperature [6] and is also believed to be nearly 100 % spin polarised at room temperature. Lastly the strontium iron oxides, $SrFeO_{3-\delta}$ which have unusual electronic and magnetic properties which are strongly linked to the oxygen content of the compound [7]. In chapter 2 we give a background of the three materials. Chapter 3 provides detailed information on the experimental procedures used to produce and characterise thin films of the three different materials. Chapter 4 presents a study on un-doped titanium dioxide. A study on cobalt doped titanium dioxide is presented in chapter 5, showing the effect of growth parameters including substrate choice and cobalt concentration on the structural, magnetic and optical properties of the films. Chapter 6 presents the growth and characterisation of the double perovskite, Sr_2FeMoO_6 and chapter 7 presents a small investigation on $SrFeO_{3-\delta}$, where the material is prepared under various conditions in an attempt to obtain a variety of oxygen phases.

Chapter 2

Background

This chapter is an introduction to the three materials studied in this thesis, namely cobalt doped titanium dioxide, the double perovskite, Sr_2FeMoO_6 and the strontium iron oxides, $SrFeO_{3-\delta}$.

2.1 Cobalt doped titanium dioxide, Co:TiO_2

Materials that exhibit both ferromagnetic and semiconducting properties, known as magnetic semiconductors, have received considerable interest for their potential applications in spintronic devices. If implemented in practical devices magnetic semiconductors would be able to control both the charge and the spin state of the carriers, where as conventional devices are only able to utilise charge. For magnetic semiconductors to be practical they need to be compatible with existing circuit technology, which is why there has been much research into dilute magnetic semiconductors. Dilute magnetic semiconductors are composed of a semiconducting host doped with a transition metal. The benefit of these materials over magnetic semiconductors is that they can be matched in conductivity to non

magnetic semiconductors and also have similar lattice parameters, allowing multilayers of ferromagnetic and non-ferromagnetic semiconductors to be synthesised with no defect states at the interface.

The dilute III-V magnetic semiconductors have been intensively researched and presently Mn doped GaAs is probably the most promising candidate for practical applications. Thin films of Mn:GaAs have been shown to be ferromagnetic up to 110 K and it has been shown that the ordering temperature is optically tuneable. To make practical spintronics devices a ferromagnetic semiconductor with a Curie temperature of ~300 K is required and despite researchers best efforts the Curie temperature of Mn:GaAs films remains well below room temperature [8]. Another disadvantage of Mn:GaAs and other Mn doped III-V systems, is that the carriers are holes and in most semiconductors, electrons have considerably shorter spin flip scattering times than holes, making n-type materials more desirable for practical spintronic applications, where low resistivities are important.

One such material is cobalt doped titanium dioxide which has received widespread interest since it was discovered to be ferromagnetic at room temperature by Y. Matsumoto *et al* [9]. In addition to its magnetic properties Co:TiO_2 has a wide indirect band gap and is transparent in the optical and near-infrared, making it desirable for optoelectronic applications.

Un-doped titanium dioxide appears in three different crystal structures, rutile, anatase and brookite. Rutile is a tetragonal structure (figure 2.1) and is the

most energetically stable crystal phase of TiO_2. Anatase is also a tetragonal structure (figure 2.1) and is difficult to obtain in bulk due to being less thermodynamically stable than rutile. It is however, readily obtainable as a thin film, although it is only metastable and undergoes an irreversible transition to rutile at temperatures above ~800 ^{o}C. The third crystal phase, brookite has an octahedral structure, it is only obtained under extreme conditions and is very unstable. In un-doped TiO_2 the lattice consists of Ti^{4+} atoms bonded to O^{2-} atoms. When doped with cobalt it is thought that Co^{2+} atoms substitute on Ti^{4+} sites [10,11], creating stable oxygen vacancies in the host lattice. However, it is not certain if the vacancies are created around Ti or Co atoms.

Although Co:TiO_2 was discovered to exhibit room temperature ferromagnetism in 2001, the exact mechanism responsible for the ferromagnetism in Co:TiO_2 is still hotly debated. There is considerable concern that the cobalt does not substitute into the TiO_2 lattice, preferring to form nanoclusters within the

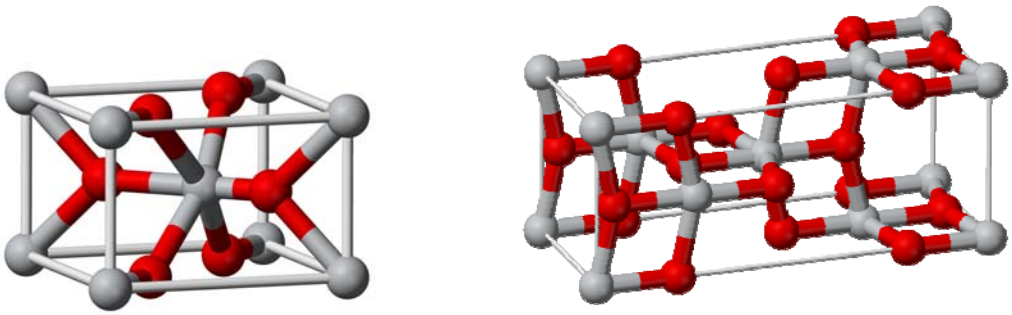

(a) (b)

Figure 2.1: Sketches showing the arrangement of titanium (dark grey) and oxygen (light grey) atoms in the (a) rutile and (b) anatase TiO_2 crystal structures.

host lattice [3,12,13], leading many researchers to claim the ferromagnetism seen in $Co:TiO_2$ originates from these cobalt nanoclusters, or cobalt based impurities. This idea is supported by researchers' inability to report consistent values for the Curie temperature of the material, with groups reporting values from 400 K up to 800 K [14,15]. Cobalt clustering is undoubtedly present on the samples of some groups, S. R. Shinde *et al.* detected ~50 nm clusters by scanning transmission electron microscopy (figure 2.2) and electron-energy-loss spectroscopy of the clusters confirmed a high concentration of cobalt was present [15]. The difficulty in detecting small cobalt clusters below ~4 nm has led many to question the results of those who claim to see intrinsic magnetism in their samples.

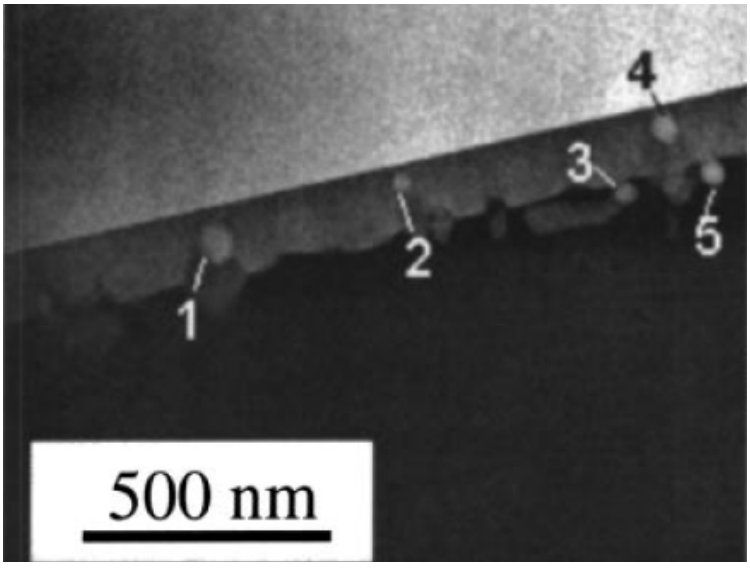

Figure 2.2: Image of cobalt nanoparticles in a $Co:TiO_2$ film grown using pulsed laser deposition by S. R. Shinde *et al.* [15]

Initially, theories to explain intrinsic ferromagnetism in Co:TiO_2 supported a superexchange interaction that is often used to explain magnetic behaviour in insulators [16]. Another more popular model is the Ruderman-Kittel-Kasuya-Yoshida (RKKY) interaction, which is a carrier mediated exchange interaction that is able to operate over a long range. This models predicts that interactions between the localised cobalt moments are mediated by delocalised electrons, leading to coupling between the cobalt moments. The strength of the coupling is inversely proportional to r^3, where 'r' is the distance between the moments. Even though the strength of the coupling follows a cubic relation, this is often enough for a cobalt moment to couple with several nearest neighbour moments, which could explain the ferromagnetic behaviour. There is also strong evidence that oxygen vacancies play a crucial role in the ferromagnetism, with many researchers reporting the saturated moments of their samples to increase with oxygen vacancies. It has recently been discovered that room temperature ferromagnetism is obtainable in un-doped TiO_2 films [17,18], which suggests that the oxygen vacancies created by the cobalt atoms rather than the cobalt atoms themselves are responsible for the ferromagnetism. In stoichiometric TiO_2 the valence of the Ti atoms is Ti^{4+} and it is non-magnetic. However, charge imbalances created by oxygen vacancies could generate Ti^{3+} and/or Ti^{2+}, which could lead to a magnetic moment. It has also been suggested that the magnetic order could originate from the oxygen vacancies themselves via d^0 magnetism. This theory suggests that the oxygen vacancies behave as an n-type dopant, acting

like electron donors. Despite intensive research the exact mechanism for the ferromagnetism in Co:TiO_2 is still controversial.

2.2 Double perovskite, Sr_2FeMoO_6

The structure of the double perovskite Sr_2FeMoO_6 (SFMO) is composed of Sr^{2+} ions and alternating octahedra of FeO_6 and MoO_6 (figure 2.3).

An interesting property of SFMO is its half metallic density of states in the electronic band structure. While there is some debate as to the valence states of the Fe and Mo ions, Fe^{3+} and Mo^{5+} are thought to be dominant [19]. In the ground state of stoichiometric SFMO the majority band is filled with localised $Fe^{3+}3d^5$

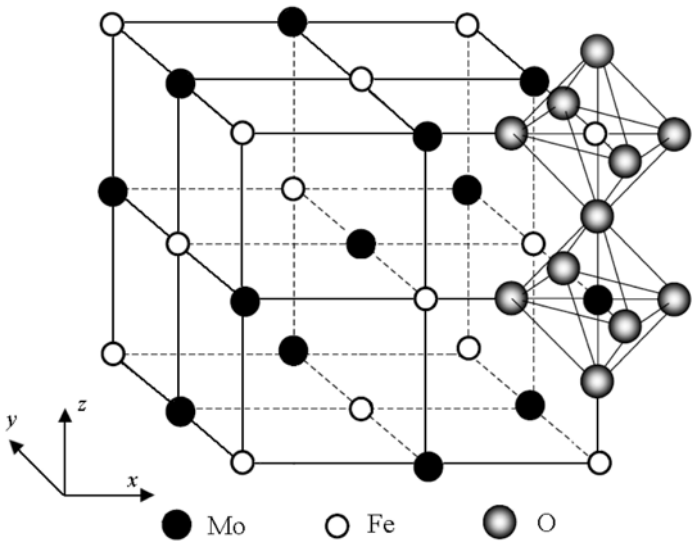

Figure 2.3: Sketch of the double perovskite Sr_2FeMoO_6 crystal structure. The strontium ion (not shown) is located at the centre of each unit cell.

spin-up electrons, while the conduction band is partially filled with delocalised $Mo^{5+}4d^1$ spin-down electrons. This half-metallic nature gives rise to 100 % spin polarised charge carriers at the Fermi energy. In addition SFMO has a high Curie temperature, in the range of 410 to 450 K [20,21,22] making it an ideal candidate for spintronic applications.

There are two main models which account for the ferrimagnetism observed in SFMO. It has been argued that a double-exchange could occur, which has been used to describe the ferromagnetism seen in Fe_3O_4 and the manganites [23,24]. This theory would account for the observed increase in Curie temperature with carrier concentration in SFMO when La^{3+} is partially substituted onto Sr^{2+} sites [25]. There is however a strong argument against this model. Because the Fe $3d^5$ orbitals are full, it has been argued that by Hund's rule, coupling cannot occur between the spin-down Mo $4d^1$ electrons and the localised spin-up $3d^5$ electrons on the Fe site [26]. In addition the spins of the $4d^1$ and $3d^5$ electron are in the opposite direction which is inconsistent with the double-exchange model.

In another model it is assumed there is an antiferromagnetic coupling between the Fe $3d^5$ and Mo $4d^1$ electrons. This model predicts a magnetic moment of 4 μ_B/f.u. (Bohr magnetons per formula unit) at low temperatures. Researchers generally do not obtain such values, instead achieving more modest moments of 2 to 3.6 μ_B/f.u. [21,27]. The discrepancy in the observed values is thought to originate from anti-site disorder [28], where a Fe^{3+} ion occupies a Mo^{5+} lattice site and vice-versa. This disrupts the alternating pattern of Fe and Mo ions creating

situations where two Fe or Mo ions occupy adjacent sites in the lattice. Although the exact effects of anti-site disorder are unknown, it has been observed to play a significant role in the magnetic properties of SFMO.

One of the more interesting properties of SFMO from a practical standpoint is its large magnetoresistance. The Magnetoresistance is defined as the change in resistance, R in the presence of an applied field,

$$MR = \frac{R(H) - R(0)}{R(0)} \tag{2.1}$$

Where R(H) is the resistance with a field applied and R(0) is the resistance in the absence of an applied field. The theoretical maximum MR of SFMO at zero Kelvin is -50 %. Actual measurements of the MR of SFMO samples in high fields have shown MR values approaching this maximum, where values of -10 % at room temperature and -40 % at liquid helium temperature have been observed. Even at low fields (1 Tesla) and room temperature, magnetoresistances of ~-5 % have been detected. The MR observed at low fields is thought to relate to the grain boundaries. It has been shown that by decreasing the size of grains, and thus increasing the number of grain boundaries the magnetoresistance is increased. It is also noted that significant low field MR has only been seen in polycrystalline films and is notably absent in single crystal samples, further evidence that grain boundaries are responsible for the observed MR at low field. It is thought the effect arises from spin polarised tunnelling between the grains. When a field is applied the magnetic orientations of adjacent grains align parallel to the field

which makes it easier for the charge carriers to tunnel between the grains due to a decrease in spin scattering, which results in a decrease of the resistivity, as observed in the experimental results. Anti-site disorder of the Fe and Mo ions has also been observed to have an effect on the MR, where increased order near the grain boundaries is believed to make it easier for charge carriers to tunnel between grains [29].

2.3 Strontium iron oxide, $SrFeO_{3-\delta}$

The Transition metal oxides ABO_3 contain an alkaline-earth ion, A and a transition metal, B surrounded by oxygen octahedra (figure 2.4). They have been extensively studied for many years, largely due to the discovery of the cuprate superconductors and colossal magnetoresistance in the manganites. Competing charge and orbital ordering in the manganites result in some interesting magnetic and transport properties. For example, the manganite $LaMnO_3$, is an antiferromagnetic insulator which shows a co-operative Jahn-Teller effect [30], while its ferrate counterpart, $SrFeO_3$ shows no sign of Jahn-Teller distortion, remaining metallic and cubic down to 4.2 K [31]. The various oxygen phases of $SrFeO_{3-\delta}$ are actively being researched as it is thought they may provide insight into other perovskite systems, including Sr_2FeMoO_6, as nano-phases of $SrFeO_{3-\delta}$ appear on SFMO films that have high anti-site disorder. $SrFeO_{3-\delta}$ is also of interest for applications, where it may be able to form antiferromagnetic-ferromagnetic

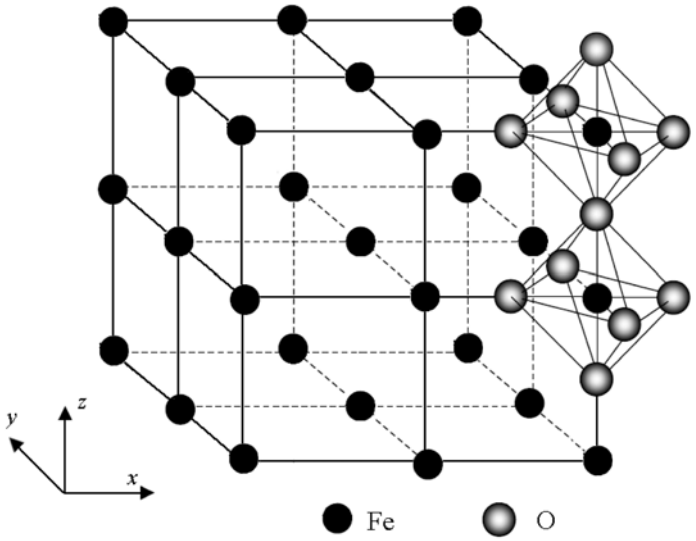

Figure 2.4: Sketch of the $SrFeO_3$ crystal structure. The strontium ion (not shown) is located at the centre of each unit cell.

multilayers with SFMO, as both materials have very similar lattice parameters. The complex and competing exchange interactions in the ferrates are also of interest from a pure physics prospective.

The material $Sr_2FeO_{3-\delta}$ is thought to exist in four different oxygen phases within the range of $3-\delta = 2.5 - 3$ [32]. The cubic $SrFeO_3$ ($3-\delta = 3$), tetragonal $Sr_8Fe_8O_{23}$ ($3-\delta = 2.875$) and the orthorhombic phases, $Sr_4Fe_4O_{11}$ ($3-\delta = 2.75$) (figure 2.5) and $Sr_2Fe_2O_5$ ($3-\delta = 2.5$). Evidence from Mössbauer measurements suggests these are the only stable phases that exist in this range [33,34] and stoichiometries other than these are an inhomogeneous mixture of the four phases.

The cubic phase $SrFeO_3$ has helical antiferromagnetic order at ~140 K and is highly conductive. It consists of well ordered FeO_6 octahedra where the Fe ions

have 4+ valence. By reducing the oxygen content we can obtain $Sr_8Fe_8O_{23}$. This phase shows antiferromagnetic order at ~70 K and displays an order of magnitude increase in resistivity below this temperature. The phase is made up of square pyramidal FeO_5 which form dimers. These are adjacent to distorted FeO_6 and well ordered FeO_6 octahedra. It is argued that the Fe ions in the distorted FeO_6 octahedra have a valence of 3.5+ while the other Fe ions are both 4+. The increase in resistivity is thought to be caused by charge ordering of the $Fe^{3.5+}$ ions to Fe^{3+} and Fe^{4+} [34,35] reminiscent of the partial charge ordering Verwey transition in Fe_3O_4. Further reduction in oxygen content leads to the $Sr_4Fe_4O_{11}$ phase, that is antiferromagnetic below ~230 K and shows semiconductor like resistivity. It contains square pyramidal FeO_5 which form dimers and distorted FeO_6 octahedra. The Fe ions are believed to have valances of 3+ and 4+ respectively. The Fe^{4+} ions in the FeO_6 octahedra have antiferromagnetic order, while the Fe^{3+} ions are not believed to posses any long range magnetic order. However, there is evidence that spin-frustration in the Fe^{3+} moments can cause weak spin-glass behaviour below ~50 K [36]. The $Sr_4Fe_4O_{11}$ phase also shows an exchange bias like effect below ~230 K, which is well above the temperature where the spin-glass behaviour is observed. The magnetic ordering temperature of the Fe^{4+} ions is around 230 K, suggesting they play a key role in the mechanism causing the exchange bias like effect. Finally there is the oxygen deficient, $Sr_2Fe_2O_5$ phase. It has the brownmillerite structure and is composed of FeO_4 tetrahedra and distorted FeO_6 octahedra, where the Fe ion is believed to have a valence of 3+.

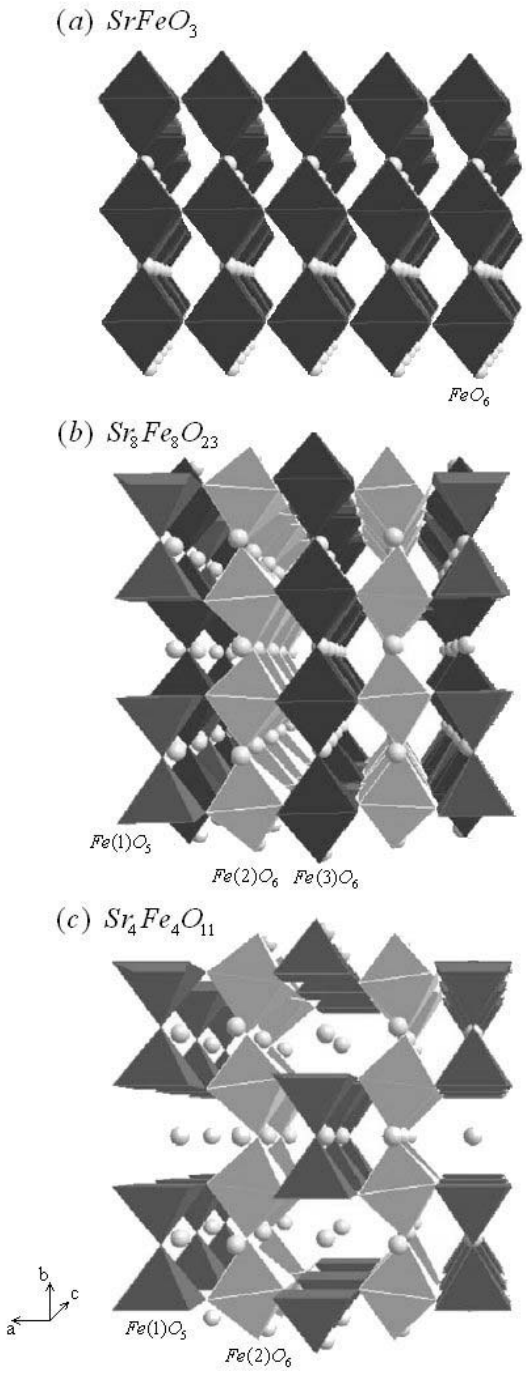

Figure 2.5: Crystal structures of (a) $SrFeO_3$, (b) $Sr_8Fe_8O_{23}$ and (c) $Sr_4Fe_4O_{11}$. Well ordered FeO_6 octahedra are shown in black, FeO_5 dimers are shown in grey and distorted FeO_6 octahedra are shown in light grey.

Chapter 3

Experimental background and details

This chapter outlines the methods of producing cobalt doped titanium dioxide, double perovskite and strontium iron oxide thin films. Details of the equipment used to characterise the structural, optical and magnetic properties of the samples are also presented.

3.1 Pulsed Laser Deposition (PLD)

Pulsed laser deposition is a relatively simple method of growing films. High energy laser pulses are focused onto a target material. These pulses are absorbed by the target material creating electronic excitation. This energy quickly converts to other forms, including kinetic energy and heat, resulting in ablation of the target, which ejects a plume of ionized particles. By controlling the geometry of the laser beam and target, it is possible to direct the path of the plume, creating a thin film on the desired substrate surface. The creation and expansion of the plume is a very complex process with many competing mechanisms. During the growth of the film, both the target and substrate are held in vacuum. This ensures

the ejected material does not interact with air, preventing scattering of the plume and the deposition of unwanted species on the substrate.

Growth techniques such as Molecular Beam Epitaxy (MBE) require the target material to be molten; this excludes certain materials with high melting points from being used in MBE and other similar methods. PLD however allows a solid target to be used, and thus a greater variety of material to be grown. Pulsed laser deposition has also been found to be very useful for creating thin films of oxides because the growths are performed in a sealed chamber and it is a simple procedure to introduce a background gas during growth. By varying the oxygen pressure of the background gas a level of control is afforded on the oxygen content of the resultant film.

One of the main disadvantages of PLD growth is the production of particulates. These are formed at the laser-target interface where the target material is ejected, creating a plume of material containing electrons, ions, molecules and often undesirable particulates including large clusters and molten globules. While there are methods to reduce and even eliminate particulates, they are still found on many films grown by PLD. Another disadvantage of using PLD is the angular nature of the plume, which is conical in shape. This gives a non-uniform deposition of material, creating films with thickness gradients that decrease as the deposition site moves further away from the plume centre. These two main drawbacks preclude large-scale production and hence commercialisation of PLD, leaving research as the primary application of the technique.

The PLD lab housed in the Department of Physics and Astronomy at the University of Canterbury consists of two vacuum chambers, an ultra high vacuum chamber and a High Vacuum chamber (HV chamber). All growths in this thesis have been undertaken in the HV chamber (figure 3.1). The chamber is cylindrical in shape and the top surface is a removable lid which allows easy access to all components within the chamber and is sealed by an o-ring which runs around the circumference of the chamber. A Lambda Physik COMPex 205 (KrF) excimer laser situated in the same room as the chamber is used as the excitation source during growth. KrF is the highest gain system for electrically discharged pumped

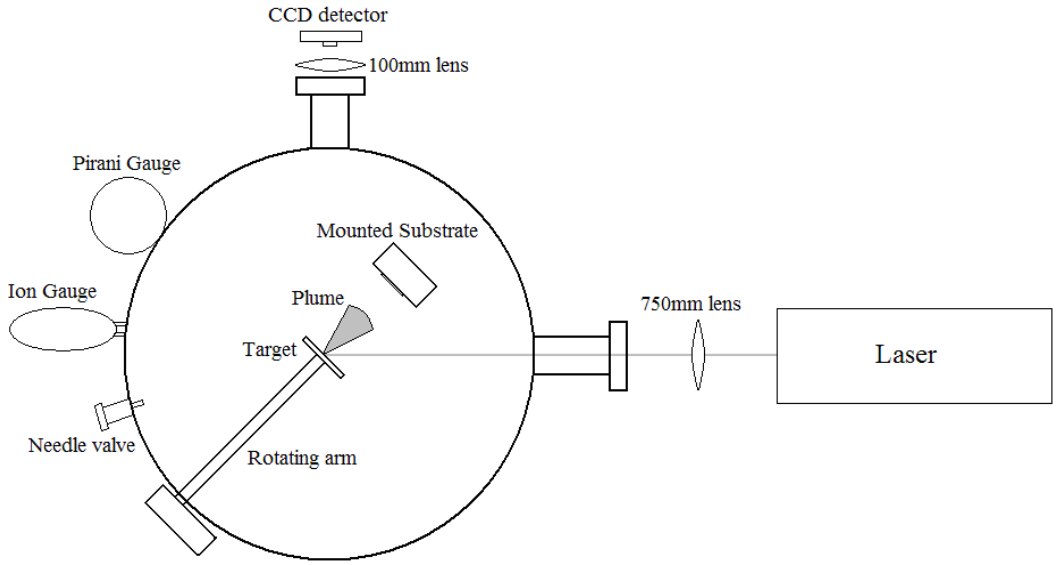

Figure 3.1: Diagram of the pulsed laser deposition set up

excimer lasers and is a popular choice amongst PLD users. The laser emits 25 ns pulses at a wavelength of 248 nm and was set at a pulse frequency of 10 Hz for all growths.

The target was mounted between two circular stainless steel plates; the front plate having a hole in the centre, which exposed the majority of the target. The beam of the laser was focused onto a non-centralised spot of the target using a 750 mm quartz lens. Quartz was used due to its high transmission of UV. The lens also had an anti-reflective coating to further increase transmission. The focused laser beam was at a 45 degree angle to the target surface. To expose more of the target to the laser, a stepper motor operating at 0.89 Hz was used to rotate the target during growth. This led to circular tracks of ablated material in the target after growth.

To collect the ablated material, various substrates were mounted with silver paste onto a heater. The silver paste acts not only as an adhesive but also provides good thermal contact between the heater and substrate. The heater was placed opposite the target, normal to and in the path of the ejected plume. A variety of substrates where used during this thesis including sapphire, silicon and $SrTiO_3$. The substrate choice is one of the key parameters in PLD growth, where substrate choice can dictate the crystal formation the film adopts during deposition. The heater temperature was controlled and monitored during growth, with temperatures from 550 to 850 ^{o}C being used. By heating the deposition surface the

ablated species is able to more easily diffuse on the surface, which can improve film quality and also encourage the formation of a desired crystal structure.

The chamber has two pressure gauges, the Pirani gauge that records pressures down to ~5 mTorr and the Duniway I-100-K ion gauge. The ion gauge is connected to a Stanford Research System IGC100 controller, which is capable of reading the lowest pressures achievable in the HV chamber, but does not operate above pressures of ~0.5 mTorr. Unfortunately this leaves a region from 0.5 to 5 mTorr where accurate pressure readings are not obtainable. A jump in pressure is observed during the start of successful ablation of a target material (figure 3.2). The size of the jump can be used as a rough indication of the density of the plume, allowing for a last minute alteration of the laser energy to increase or decrease the plume density. The chamber was evacuated using a two-stage pumping system. A diaphragm pump was used to bring the pressure down to around 1 Torr, at which stage a Turbo-molecular pump was activated that generated chamber pressures around 5×10^{-6} Torr. Most growths in this thesis were performed in a background oxygen gas, with pressures from vacuum up to 80 mTorr being used.

The samples in this thesis are labelled PLD‘XX’_‘Y’, where ‘XX’ represents a unique substrate and film composition and ‘Y’ represents different films with the same substrate and film composition. For example in this thesis, XX = 39 represents a TiO_2 film deposited on sapphire, hence PLD39_3 represents the third TiO_2 film grown on a sapphire substrate.

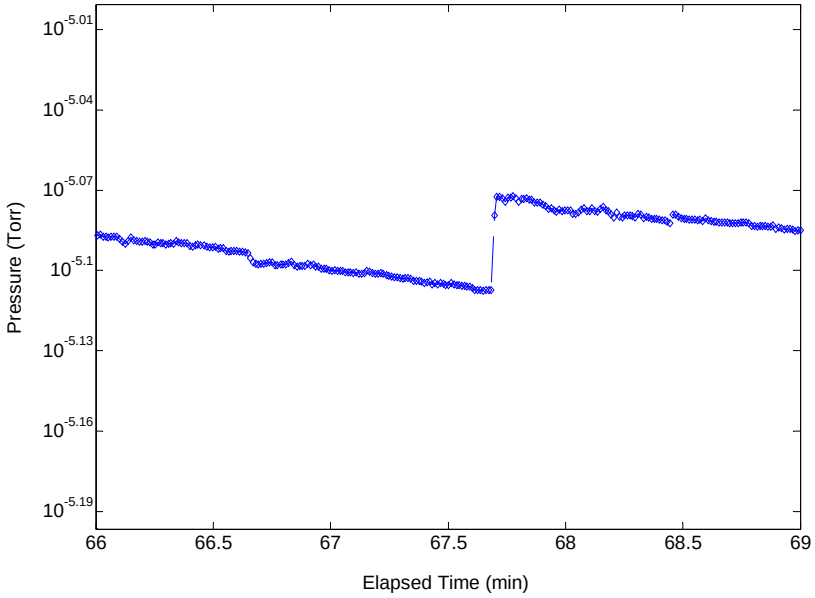

Figure 3.2: Pressure change observed at the start of ablation.

3.2 Target preparation

All targets unless otherwise stated, were produced by Dr. Grant Williams at Industrial Research Limited.

3.2.1 Co:TiO_2

Six different targets were used for the growth of Co:TiO_2 films. Two un-doped Ti and TiO_2 targets were purchased from Kurt. J. Lesker, both better than 99.99 % purity and the remaining targets where produced by Dr. Grant Williams, who made three Co:TiO_2 targets from mixes of 99.99 % pure TiO_2 powder and 1μm cobalt oxide powder. Prior to mixing, the TiO_2 was ground with a mortar and

pestle until the particle size was 2-5 micron. Once the TiO_2 was ground the cobalt oxide was added and ground until the cobalt could be assumed to be uniformly distributed throughout the TiO_2 powder. The powder was then pressed with a die at 40 000 kPa, forming circular pellets roughly 8 mm in diameter. The pellets were then placed in a crucible and loaded into a furnace for cooking. X-ray diffraction measurements of initial attempts, where the pellets were cooked in air, showed large amounts of $CoTiO_3$, which is an undesirable impurity phase. It was found that by filling the furnace with nitrogen, the $CoTiO_3$ in the resulting target could be reduced by over 80 % (figure 3.3). To reduce impurities in the films, Co:TiO_2 targets used in this thesis were all cooked in nitrogen at 1222 ^oC for 6 hours. The high temperatures were needed to increase the density, as low density PLD targets produce poor films with large amount of particulates [37]. After cooking, the pellets were left in the furnace to cool to avoid cracking from thermal shock. This method was used to create three targets with 3, 6 and 12 % cobalt concentrations that will be referred to as Co(3%):TiO_2, Co(6%):TiO_2 and Co(12%):TiO_2, respectively. There was also one other target that was made from a wet-chemical precursor of Co:TiO_2 doped with 3 % cobalt. The precursor was provided by Dr. Tim Kemmitt from Industrial Research Limited. In this instance the wet-chemical precursor was ground with the mortar and pestle and once the particle size was 2-5 micron it was cooked in the same conditions as the other pellets. This target will be referred to as wet-Co(3%):TiO_2.

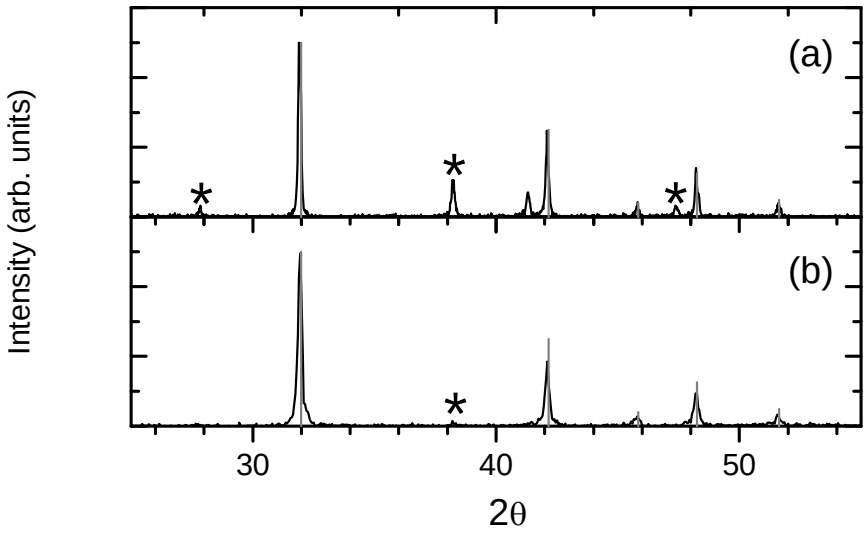

Figure 3.3: XRD data for Co:TiO_2 targets (a) annealed in air and (b) annealed in nitrogen (both have 3 % cobalt concentrations). Peaks corresponding to the $CoTiO_3$ impurity phase are indicated by a star, while the expected rutile peaks are shown by solid grey lines.

3.2.2 Sr_2FeMoO_6

A single Sr_2FeMoO_6 target was used for growing SFMO films in this thesis. The target was made from a stoichiometric mix of $Sr(NO_3)_2$, Fe_2O_3 and MoO_3 powder, which was ground together with a mortar and pestle and heated in air at 700 ^oC for 1 hour, to remove water of hydration and nitrogen from the sample. The powder was then pressed at 40 000 kPa into a pellet using a die and then loaded into a furnace and cooked in air at 1050 ^oC for 3 hours. At this stage, XRD of the pellet showed the preliminary phases, $SrMoO_4$ and $SrFeO_3$. The pellet was then ground up using the mortar and pestle, re-pressed and cooked a second time at

1200 ^{o}C for 3 hours in a 4 % H_2, 96 % N_2 atmosphere. The sample was then ground, re-pressed and cooked for a third time at 1250 ^{o}C for 3 hours in the H_2/N_2 atmosphere. After all cooks the temperature was slowly ramped down and the target was only removed when the furnace was ~100 ^{o}C to prevent decomposition and any cracks from thermal shock.

The cook in air was found to produce a pellet which was denser and more stable in ambient atmosphere over time [38]. While the repeated cooks in H_2/N_2 atmosphere removed the preliminary phases of $SrMoO_4$ and $SrFeO_3$ and increased the homogeneity of the sample. XRD of the resulting pellet showed the cubic phase to be dominant, although there was some tetragonal distortion caused by the high cooking temperatures. However, the high temperatures were necessary to make the targets sufficiently dense to be used for pulsed laser deposition.

3.2.3 $SrFeO_{3-\delta}$

A single $SrFeO_{3-\delta}$ target for PLD was synthesised from a stoichiometric mix of $Sr(NO_2)_3$ and Fe_2O_3. The powders were ground by mortar and pestle, de-nitrated in air at 700 ^{o}C and then pressed at 40 000 kPa into a pellet. The pellet was sintered at 1050 ^{o}C in air for 24 hours and the furnace was allowed to cool to ~100 ^{o}C before the sample was removed. The pellet was then ground and re-sintered at 1200 ^{o}C for a similar duration. This process was repeated once more with the final sinter done at 1250 ^{o}C, ensuring a dense target with good homogeneity.

To load the pellet with oxygen it was placed in an oxygen rich furnace for 24 hours and heated to 700 ^{o}C. This allowed the oxygen to diffuse through the pellet and increased the density. The pellet was then cooled to 400 ^{o}C where it was left for another 24 hours, before being slowly cooled to room temperature and removed from the furnace. The slow cooling reduced thermal shock and ensured no cracks formed in the target. XRD measurements showed the target structure to be cubic, indicating a high oxygen content with $3-\delta \sim 2.95$.

3.3 X-Ray Diffraction (XRD)

X-ray diffraction is a non-destructive technique which was used to find the chemical composition and crystallographic structure of each sample. When a monochromatic X-ray beam (with wavelength, λ) is projected onto a crystal lattice at a certain angle, θ, diffraction only occurs when the distance between successive lattice spacings in the beams path differs by a complete number of wavelengths. This is shown by Bragg's Law,

$$n\lambda = 2d\sin\theta \tag{3.1}$$

Where n is an integer and d is the interplanar spacing. Scanning over the angle theta and plotting theta against the resulting intensity results in a diffractogram, which is characteristic of the sample.

The diffractometer used was a Bruker D8 Advance located at Industrial Research Limited, with an incident beam goebel mirror and a 0.23 degree parallel

plate diffracted beam collimator. The operating voltage was 40 kV and the current was 35 mA. Cobalt Kα, which has a wavelength of 0.1789 nm was used as the radiation source. For highly oriented samples the crystal must be oriented with the incoming beam to a high degree of accuracy. In the D8 diffractometer the sample is mounted horizontally and the angle of the radiation Tube and the detector are able to be controlled independently. This allows the D8 to align the Tube and detector normal to the surface of crystallographic planes in a sample.

A number of different scans were performed on the samples. Scans over the angle theta were used to find the composition and crystal phases of the films. To assess the level of orientation of various film peaks rocking curves were done. This is where the tube and detector are positioned so that a specific crystal orientation is at its maximum intensity, the tube and detector are then both 'rocked' simultaneously, while holding theta constant. The FWHM of the resultant peak gives a good indication of the level of orientation of the crystal peak. The more oriented a crystal phase is the sharper the rocking curve peak will be. A final measurement known as grazing incidence was performed on some samples. This technique involved setting the radiation tube at a very low angle with respect to the sample surface. The detector tube is then scanned over a wide range of angles. This increases the sampling area but does not receive signal from any oriented crystal phases, allowing the detection of unorientated impurity phases which give very weak signals. Measurements of the samples were analysed using the Eva software and the chemical composition and crystallographic

structure were identified using the International Centre for Diffraction Data database.

3.4 Microscope photography

An Olympus BX60M microscope situated in the X-ray diffraction lab of Industrial Research Limited was used to view the samples at high magnifications. An Olympus colour view camera which was integrated into the microscope, allowed high magnifications images of the samples to be taken. The images where saved directly onto a computer using the analySIS imager software package. The microscope had lens objectives ranging from 5x to 100x, that give effective magnifications of around 50 to 1000. Images of all samples where taken at 50 and 200 times magnification. Higher magnifications were hard to focus and offered little insight into the structure of the sample surface beyond what was seen at the lower magnifications.

3.5 Scanning Electron Microscopy (SEM)

Scanning electron microscopes, as their name suggests, are a type of microscope that take advantage of electrons to obtain highly magnified images of their subject material. This is done by scanning a high energy beam of electrons across the sample surface. Secondary electrons which are emitted near the sample surface are then collected by a detector. An image is displayed that is brighter in regions

where more secondary electrons are detected. More secondary electrons tend to be emitted near edges and steep slopes, which gives SEM images their characteristic three dimensional appearance. Because electrons are being used to view the sample it is necessary for the sample to be conductive. Non-conductive samples can still be viewed with an SEM, but they require a thin layer of conductive material (gold is often used) to be deposited on their surface, prior to examination.

In this thesis two scanning electron microscopes were used, a Raith 150 located at the University of Canterbury and a LEO 440 housed at Industrial Research Limited. Both machines held the sample in vacuum while analysing the surface and despite the Raith 150 being primarily used for lithography, the machines had similar resolutions of around ~50 nm. Images taken on these machines were typically magnified between 1 000 and 50 000 times.

3.6 Rutherford backscattering spectrometry

Rutherford Backscattering Spectrometry (RBS) was used to determine the chemical composition and the film thickness of the samples. The technique uses a particle accelerator to inject He^+ ions into the surface of a sample at energies of 2 MeV, resulting in elastic backscattering of the incident beam off the target nuclei. The backscattered He^+ ions are collected in a detector that measures their energies and angle of scattering. The He^+ ions lose energy in two ways; scattering off the sample nuclei and small angle scattering with the electrons in the sample.

Different elements have different nuclei giving the backscattered He^+ ions characteristic energies and scattering angles which can be related to the sample composition. The thickness of the film can also be obtained by looking at the energy loss of He^+ ions which have scattered off nuclei in the substrate of the samples. An He^+ ion which has scattered off a substrate nuclei will show a characteristic energy loss. It will also show an additional energy loss from small angle scattering on the way to and from the substrate. By comparing the energy lost from small angle scattering with the density of electrons in the film it is possible to calculate the depth of the film. All RBS measurements of the samples were performed by Dr. John Kennedy at GNS Science's ion beam laboratory.

3.7 Optical transmission

Measurements of the optical transmittance of the samples were performed with a Cary 14 at the University of Canterbury and a Cary 50 at Industrial Research Limited. The Cary 14 is a dual beam spectrophotometer that can scan over wavelengths from ultra-violet, through the visible and up to near infra-red. The dual beam design utilises a single light source which it splits into two beams. One beam is passed through the sample and the other through an empty sample holder and both beams are monitored simultaneously by photomultiplier tubes. This allows the transmittance of the sample to be measured over a continuous change in wavelength. The Cary 50 is an updated version of the Cary 14 but works on

essentially the same principles. It is however able to scan over a slightly broader range of wavelengths, and has better reproducibility.

3.8 Superconducting quantum interference device magnetometer

A Quantum Design, Superconducting QUantum Interference Device (SQUID) magnetometer located at Industrial Research Limited was used for all magnetic measurements presented in this thesis. The SQUID is capable of measuring magnetic moments down to 10^{-8} electromagnetic units (emu), making it the most sensitive instrument for measuring magnetic materials. The SQUID was used to characterise the magnetic properties of ferromagnetic samples by doing field sweeps up to 60 000 Oersted (Oe) and temperature dependant measurements from 5 to 400 K. These field sweeps allowed us to measure the saturation magnetisation (M_s), remnant magnetisation (M_R) and coercive field (H_c). The saturation magnetisation is the magnetisation the sample achieves when the applied field is sufficiently strong that all the magnetic dipoles in the sample align parallel to the applied field. When the applied field is removed from a ferromagnetic sample which has been saturated, the magnetisation of the sample will drop to a value called the remnant magnetisation, which remains indefinitely in the absence of an applied field. The magnitude of the opposing field required to reduce the magnetisation of the sample from remnance to zero is known as the coercive field.

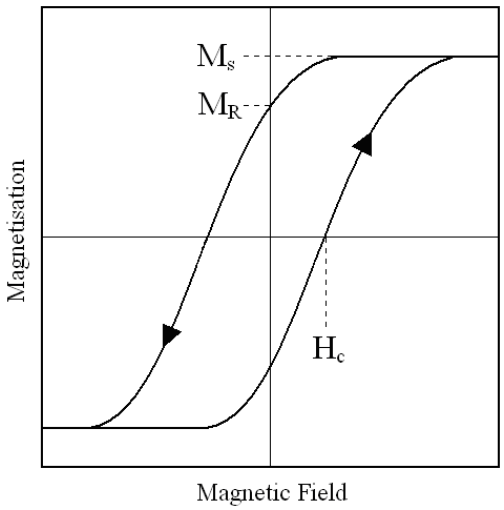

Figure 3.4: A field loop of a ferromagnetic sample showing the saturation magnetisation (M_s), remnant magnetisation (M_R) and coercive field (H_c).

The standard method for holding samples in the SQUID is to mount them in a plastic straw. While this method is effective it limits the temperature measurements to a maximum of 400 K, as the straw starts to melt above this temperature. Once the sample is mounted in the straw, it is attached to the end of a long rod, which is lowered into the detection coils housed in the SQUID. A magnet surrounding the detection coils is used to apply the field. Once the field is stable a measurement is taken by moving the sample along the symmetry axis of the detection coils. As the sample moves through the coils the magnetic dipole moment of the sample induces an electric current in the detection coils. The voltage across the coils is measured at regular intervals along the scan length and the scans are repeated up to 16 times for a single data point to increase the signal to noise ratio. The detector is made up of four detection coils in total, in a

configuration known as a second-order gradiometer. This is used to reduce the effect of any noise or offsets caused by the external magnet. When analysing data of a magnetic field scan it is necessary to subtract the diamagnetic contribution of the substrate from the magnetic moment of the sample, so that the ferromagnetic component of the film can be viewed independently. The contribution is linear so it is relatively easy to remove as long as the scan goes well past the magnetic saturation of the film, typically around 2 Tesla. Figure 3.5 shows the raw data from a field dependent scan and the data after the substrates diamagnetic contribution has been removed.

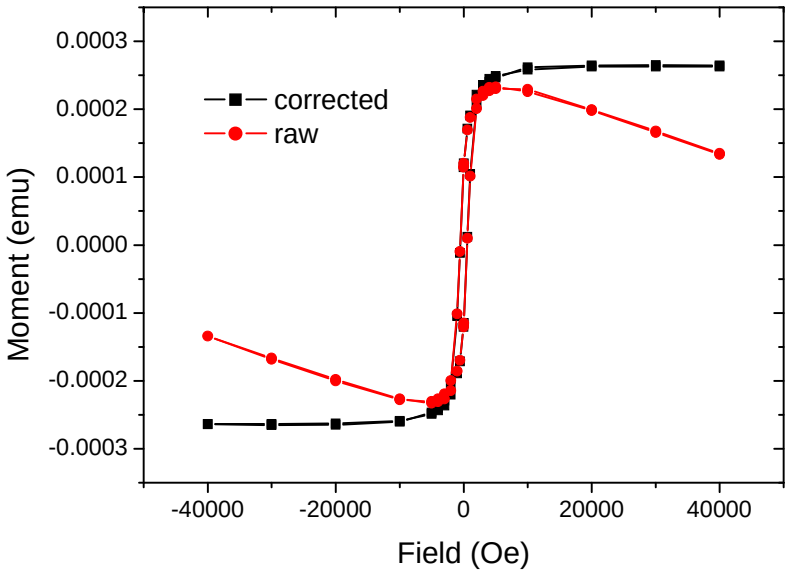

Figure 3.5: The raw data output from the SQUID for a field loop of a SFMO film grown on silicon (black line), as well as the corrected data with the substrate diamagnetism removed (grey line).

The SQUID magnetometer outputs data in the CGS system of units, recording the total magnetic moment of the sample in units of emu and the field strength in Oersted. To make the data more accessible the moment and magnetic field are converted into SI units using the following formulae,

$$Magnetisation(A.m^{-1}) = \frac{m_{emu} \times 10^3}{V} \tag{3.2}$$

Where m_{emu} is the magnetic moment in emu as measured by the SQUID and V is the volume of the film in cm^3. In this thesis we report the magnetic moment in units of Bohr magnetons per cobalt atom (μ_B/Co) for Co:TiO_2 samples and Bohr magnetons per formula unit (μ_B/f.u.) for the double perovskite samples. The moments are obtained from the magnetisation (M) using the following equation,

$$moment = \frac{M \times V_u}{\mu_B \times N} \tag{3.3}$$

Where V_u is the volume of a unit cell of the structure, N is the fraction of cobalt in the film (for SFMO and $SrFeO_{3-\delta}$ samples, N = 1) and μ_B is the Bohr magneton, a constant, with a value of 9.274×10^{-24} $A.m^2$. The film volume is obtained from measuring the area of the substrate and multiplying by the film thickness, which was estimated from RBS measurements.

3.9 Temperature dependant resistivity

We measured the resistance R of the films as a function of temperature T using a two terminal method. Contacts were bonded on to two opposing edges of the films surfaces using silver paint. To reduce voltage noise during measurements, a 12 V battery was used to apply a current across the sample. This was monitored using a Keithley 6485 picoammeter and the voltage drop across the sample was measured using a Hewlett Packard 3478A multimeter (figure 3.6). This set-up allowed us to measure Giga-ohm resistances without any deviating effects from the equipment.

Temperature dependant measurements were taken by immersing the probe that held the sample into a dewar half filled with liquid nitrogen. A CY7 series silicon diode from OMEGA, operating at a constant current of 10 μA was mounted onto the probe next to the sample and used to measure the temperature. Once the diode was below ~80 K the probe was lifted just above the liquid nitrogen and left to slowly cool in the dewar. The output voltage of the temperature diode was recorded on a Hewlett Packard 3478A multimeter and converted into a temperature measurement using a calibration table provided by OMEGA.

The resistivity of the sample was measured by alternating the direction of the current to remove the effect of any thermoelectric or voltage offsets from the

measurements. The average of the two recorded output voltages was divided by the applied current to get the resistance of the sample at the given temperature. The data was converted in real time using a program written by the summer student, Harry Jones.

The samples we measured all had rectangular geometries, which allowed us to calculate the resistivity of the films using the following equation,

$$\rho = \frac{RA}{L} \tag{3.4}$$

Where ρ is the resistivity in Ω.cm, R is the resistance in Ω, A is the cross sectional area of the film in cm^2 and L is the distance between the two contacts in cm.

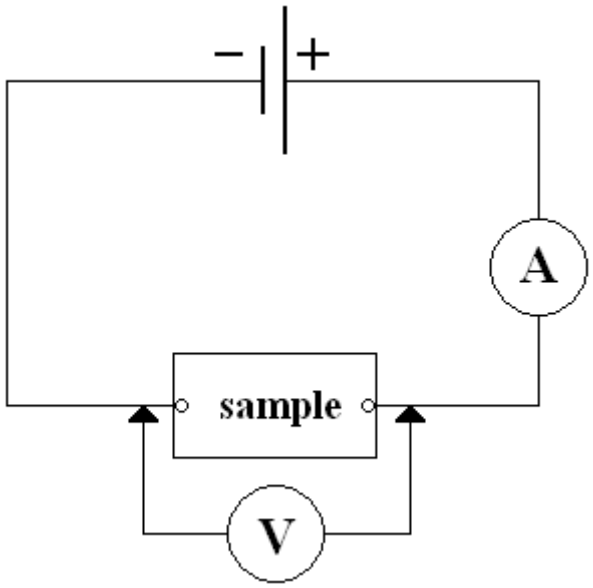

Figure 3.6: Circuit diagram of the temperature dependant resistivity set-up, showing the placement of the contacts on the sample. The picoammeter and multimeter are represented by the ‘A’ and ‘V’ components, respectively.

Chapter 4

Un-doped TiO_2

Un-doped titanium and titanium dioxide targets were used to study the effects of pulsed laser deposition growth parameters on the structural properties of TiO_2 films. Un-doped targets were mainly used due to the unavailability of Co:TiO_2 at the time. By optimising the growth parameters for un-doped TiO_2 films we hoped to achieve good quality Co:TiO_2 films later in the thesis (chapter 5).

In previous papers it has been shown that the background oxygen pressure during growth can play a large role in the formation of different crystal phases as well as the film morphology. Although researchers have had mixed results, most agree that samples grown in high oxygen pressures and at relatively low temperatures favour the formation of the anatase crystal structure, while the rutile phase is dominant at high temperatures and low oxygen pressures [39,40,41,42]. Some studies have been able to obtain single phase TiO_2 [43], while others only manage to deposit mixed crystals of rutile and anatase [44]. There is also evidence that the choice of substrate can dictate the formation of either the anatase or rutile phase [14,44,45]. To get the desired crystal phase a substrate with similar lattice parameters is chosen, thus making the formation of the desired crystal more

favourable. There are however, researchers who have found they are only able to obtain one crystal phase regardless of the variation in parameters.

4.1 Pulsed laser deposition

The first four growths of TiO_2 films investigated the effects of oxygen pressure on the structural characteristics of the resulting film. The oxygen pressure was systematically varied, while all other parameters where held as constant as possible, although the laser energy was unintentionally changed between growths due to the KrF laser running low on gas. These samples were grown on sapphire substrates using a TiO_2 target purchased from Kurt. J. Lesker.

Another four growths were performed at lower temperatures and high oxygen pressures, which are reported to favour the formation of the anatase crystal phase. However, SEM images of one of the initial samples grown at 50 mTorr showed a rough film with a high density of unwanted particulates, hence we used a modest oxygen pressure of 10 mTorr for these growths. Two different targets were used for these growths, the TiO_2 target used in the first series of growths and a Ti target (also from Kurt. J. Lesker). The laser energy was increased from 120 to 240 mJ when using the Ti target as the ablation appeared to be insufficient at the lower energy upon visual observation. A silicon substrate was loaded next to the sapphire substrate during growth so the formation of TiO_2 on the different surfaces could be compared.

For all un-doped TiO_2 growths the laser beam was focused to a 5 mm^2 spot on the target. Laser energies between 120 and 240 mJ where used, resulting in laser fluences from 0.5 to 1 J/cm^2. A summary of the other growth parameters is presented in table 4.1. Note that the sample PLD39_1 is grown in a vacuum with no background gas, while all other samples are grown at higher growth pressures by introducing oxygen into the chamber. The growth time for all the samples was 60 minutes.

Film Label	Substrate	Target composition	Growth Pressure	Substrate Temperature	Laser Fluence (j/cm2)
PLD39_1	sapphire	TiO2 (Lesker)	1E-5 Torr	700 °C	0.7
PLD39_2	sapphire	TiO2 (Lesker)	1 mTorr	700 °C	0.55
PLD39_3	sapphire	TiO2 (Lesker)	10 mTorr	700 °C	0.5
PLD39_4	sapphire	TiO2 (Lesker)	50 mTorr	700 °C	0.65
PLD39_5	sapphire	TiO2 (Lesker)	10 mTorr	550 °C	0.5
PLD42_1	silicon	TiO2 (Lesker)	10 mTorr	550 °C	0.5
PLD39_6	sapphire	Ti (Lesker)	10 mTorr	550 °C	1
PLD42_2	silicon	Ti (Lesker)	10 mTorr	550 °C	1

Table 4.1: A summary of the growth parameters used during the growth of un-doped TiO_2 films.

4.2 Structural characterisation

4.2.1 Microscope images

The samples were analysed using an optical microscope. The sample PLD39_1 was lightly coated with 'white bumps', which were possibly air bubbles showing early stages of the film lifting off. Samples PLD39_2 (figure 4.1) and PLD39_3 were very similar under the microscope, both showing the white bumps found on PLD39_1 but in higher concentrations. Both samples also showed moderate amounts of film peeling off the substrate. PLD39_4 did not show any signs of film peeling but did have a very high density of the white bumps found on the other samples, suggesting that higher growth pressures encourage the development of the white bumps.

Microscope images of the sample PLD39 _5 showed large amounts of film peeling, the sample also had the 'white bumps' observed in previous films. The microscope images of PLD39 _6 did not show any film peeling but did show a large density of white bumps. The silicon sample, PLD42_1 is purple to the naked eye and under the microscope we observed the film to be composed of large granules around 20 microns across (figure 4.1). The other silicon film PLD42_2 grown with the Ti target is completely smooth down to the resolution of the microscope (1000 times) and the sample is bright blue to the naked eye.

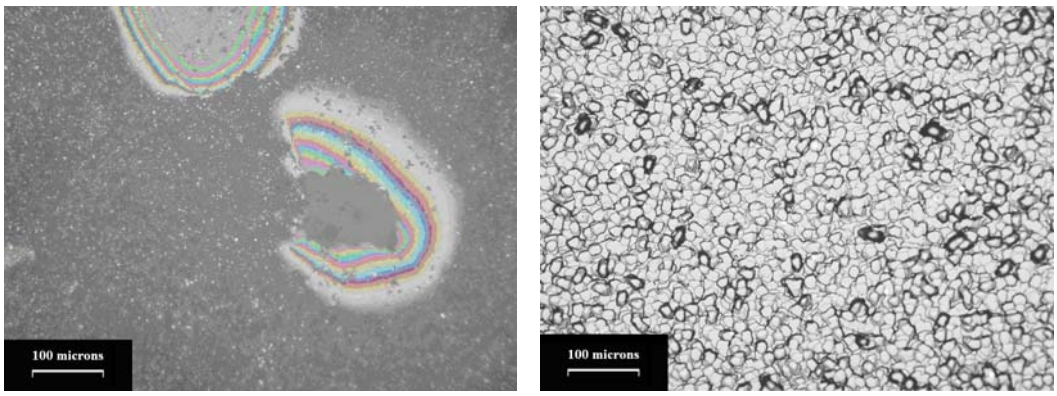

(a) (b)

Figure 4.1: (a) Film peeling observed on the sapphire sample PLD39_2. (b) Large granules seen on the silicon sample PLD41_1. Both images where taken at 200 times magnification.

4.2.2 Scanning electron microscope images

The Raith 150 scanning electron microscope at the University of Canterbury was used to take images of the samples grown in varying oxygen pressures. The SEM image of PLD39_3 grown at 10 mTorr (figure 4.2) shows the grain sizes of the film to be around 25 nm. The sample PLD39_2 grown at 1 mTorr had a slightly smaller grain size of around 20 nm and PLD39_1 grown in vacuum showed the smallest grain size of all. Although the difference in these three films was only marginal, the images suggest that higher oxygen pressures during growth result in the formation of larger grains. This was confirmed upon observation of the sample PLD39_4 grown at 50 mTorr (figure 4.2), where the grain size was around 40 nm, which is considerably larger than what was found on the other films.

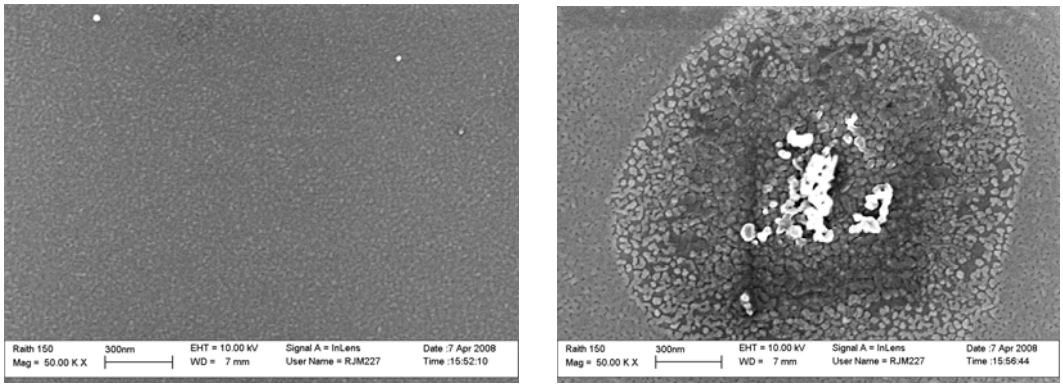

(a) (b)

Figure 4.2: SEM images of films grown in oxygen pressures of (a) 10 mTorr and (b) 50 mTorr. The images were taken at 50 000 times magnification.

At lower magnifications (1000 times) the samples grown at and below 10 mTorr had surfaces which appeared smooth and there were only a few particulates on the samples surfaces. The sample grown at 50 mTorr however, was rougher and showed areas with higher particulate density than was found on the other films. This could be an anomaly, as high oxygen pressures should not increase the density of particulates on the films.

4.2.3 X-ray diffraction

X-ray diffraction measurements of the samples were performed at room temperature using CoK_{α} radiation. The measurements confirmed the orientation of the substrates to be (004) silicon and (0001) sapphire. The samples grown on sapphire were all found to possess the rutile (200) crystal phase. Initially it was thought a small peak around 44.3^{o} observed on the shoulder of the sapphire β–

peak could be sign of anatase (004). However, when an iron foil was used to filter out the signal of the β–peak the peak assumed to be anatase (004) also disappeared. As the iron foil should not have any effect on film peaks, the peak at 44.3^{o} was obviously an artefact originating from the instrument. Scans of the silicon samples did not show any signs of film peaks. This could mean there is no film present, the film is amorphous, the film is epitaxial but aligned to the lattice planes of the substrate or most likely the film is polycrystalline, although if polycrystalline, scans would be expected to reveal some weak film peaks. Deposition of epitaxial TiO_2 on silicon is difficult as the silicon lattice has an 18 % and 43 % mismatched to rutile and anatase TiO_2 respectively.

The films deposited on sapphire substrates were found to be highly oriented and single crystal. The rutile (200) peak on the sapphire films grown at 700 ^{o}C had full width half maximums (FWHM's) of around 0.6^{o} and rocking curves of the peak were ~0.1^{o}, which is near the limit of the instrument resolution. The peak was shifted by ~0.45^{o}, indicating c-axis compression. This is expected as the sapphire a-b lattice plane is 4 % larger than in the rutile TiO_2 lattice, this would result in a tensile strain on the a-b plane and hence a compressed c-axis, although the amount of strain seems rather large for only a 4 % mismatch. The sapphire samples grown at 550 ^{o}C (figure 4.3) showed shifts of 0.65^{o} for the (200) rutile peak which is almost 50 % larger than the shift on the samples grown at 700 ^{o}C. It could be that increased diffusion at higher growth temperatures allows the film to

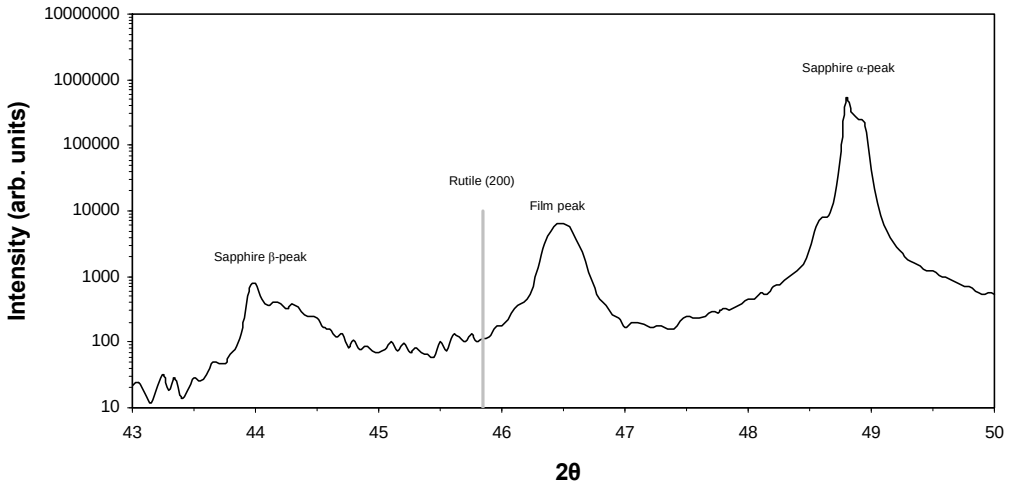

Figure 4.3: XRD scan showing the reference pattern for the (200) rutile peak and the shifted (200) rutile peak on the sapphire sample PLD39_5.

adopt a more energetically favourable lattice which would reduce the strain. The samples grown at the lower temperature where still well aligned and oriented with 0.1^{o} rocking curves on the rutile (200) peak.

4.3 Optical transmission

Optical transmission requires the film to be on a transparent substrate, for this reason no transmission data could be obtained for silicon samples. Even sapphire which is transparent can only be analysed for transmission if the substrate is polished on both sides. The sample PLD39_1 was grown on single side polished sapphire so it was unable to be measured. One side of the substrates were coated in silver paste prior to growth, which was used to bond the substrate to the heater.

The paste was removed post growth with a razor and methanol wipes. The cleaning process may have left small traces of silver paste or scratches on the surfaces which could scatter light passing through the sample, reducing the transmission of the samples.

The sapphire samples that were double side polished were measured for optical transparency using the Cary14 at the University of Canterbury. The resulting transmission spectra showed the films to be transparent across the visible spectrum (figure 4.4). From the transmission data it is possible to calculate the optical band gap, E_g of the samples from the absorption coefficient, α [46,47].

The absorption coefficient is given as,

$$\alpha = \frac{A \times \ln(10)}{d} \tag{4.1}$$

Where d is the film thickness, assumed to be 100nm (the thickness has no bearing on the calculation of E_g) and A is the absorbance, which can be directly calculated from the transmission,

$$A = -\log_{10}(Transmission) \tag{4.2}$$

The optical band gap can then be calculated using the absorption coefficient,

$$\alpha.h.v = C(hv - E_g)^n \tag{4.3}$$

where hv is the photon energy, C is an absorption constant and $n = 2$ for indirect transitions. By creating a plot with $(\alpha hv)^{1/n}$ on the y-axis and $(hv - E_g)$ on the x-axis we see that when the condition $hv - E_g = 0$ is satisfied then $hv = E_g$. Hence the band gap is found at the x-intercept of a linear extrapolation of such a plot as

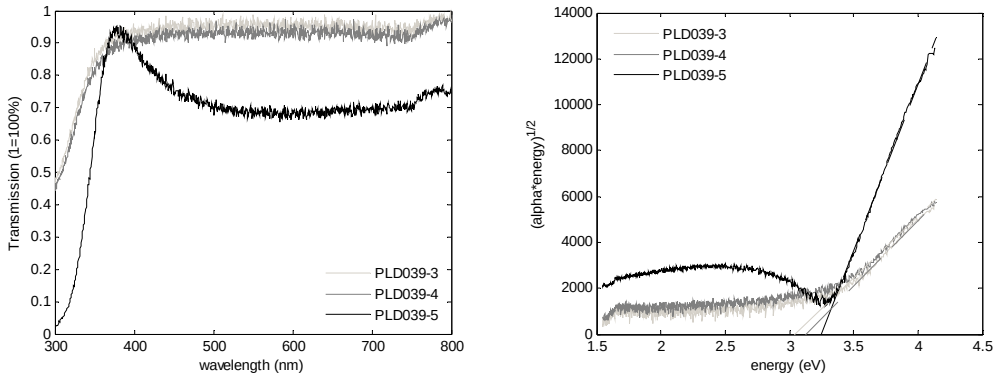

(a) (b)

Figure 4.4: Transmission data (a) and a Tauc plot (b), the dotted lines connect to the band gap energy on the x-axis. Only three samples are shown for clarity.

seen in figure 4.4(b).

The plots created using this method are know as Tauc plots. Tauc plots were created for all TiO_2 samples with transmission spectra, from which the band gaps of the samples were obtained (table 4.2). The band gaps are 3.03 eV, 3.34 eV and 3.37 eV for bulk, polycrystalline and epitaxial forms of the rutile crystal [69]. The values calculated for the sapphire samples are between those of the known bulk and polycrystalline values. Unfortunately the obtained data may have considerable errors introduced by the cleaning method of the films, which makes it difficult to ascertain any relationships between the optical properties of the film and the growth parameters used.

Film Label	Growth Pressure	Substrate Temperature	Band gap (eV)
PLD39_2	1 mTorr	700 ^{o}C	2.90
PLD39_3	10 mTorr	700 ^{o}C	3.15
PLD39_4	50 mTorr	700 ^{o}C	3.11
PLD39_5	10 mTorr	550 ^{o}C	3.26
PLD39_6	10 mTorr	550 ^{o}C	3.28

Table 4.2: Optical band gap energies calculated from transmission data

4.4 Summary

The effect of oxygen pressure and substrate temperature during growth on the structural and optical properties of TiO_2 films was studied. Microscope images of the samples showed many of them had film peeling off the substrate surface. X-ray diffraction measurements showed the films grown on sapphire to be highly oriented single phase rutile with (200) orientation and rocking curves of these samples showed the film peak to be shifted by 0.45^{o} to 0.65^{o}, where growths performed at higher temperatures were observed to have smaller shifts. Scanning electron microscope images suggest that the grain size of the films can be controlled by oxygen pressure during growth, with higher growth pressures resulting in larger grains. The optical band gaps calculated from the transmission data ranged from 2.9 to 3.3 eV.

Chapter 5

Co:TiO_2

Since the discovery of room temperature ferromagnetism in Co:TiO_2 films by Matsumoto *et al*. [9] researchers have debated the magnetic nature of Co:TiO_2. Some researchers have concluded the ferromagnetism is intrinsic, arising from either carrier induced interactions between the cobalt atoms, or from the oxygen vacancies that are stabilised by the dopant cobalt atoms. There is however, evidence that cobalt tends to segregate in Co:TiO_2 films rather than incorporating into the host lattice, resulting in the formation of cobalt clusters. It has been argued that these clusters, rather than any intrinsic mechanism are responsible for the observed magnetism.

In this chapter we investigate the role of the cobalt dopant on the TiO_2 lattice by growing films doped with varying concentrations of cobalt. In addition, the growth parameters used in chapter 4 are further optimised with the introduction of post growth annealing. In an attempt to obtain the anatase crystal phase of TiO_2, films were grown on strontium titanate ($SrTiO_3$) substrates, which lattice match the anatase phase of TiO_2 to within 3 %. Twenty Co:TiO_2 samples

were prepared by the PLD method, the results of structural, optical and magnetic measurements of the samples are presented here.

5.1 Pulsed laser deposition

For initial growths we continued to use the two growth 'regimes' seen in chapter 4, 700 ^{o}C in 0.2 mTorr of oxygen pressure thought to favour rutile and 550 ^{o}C with 10 mTorr oxygen pressure thought to favour the formation of anatase. We also started annealing samples in vacuum for 1 hour immediately after growth. This was done to increase oxygen vacancies and to improve the homogeneity of the samples. The Co:TiO_2 targets used for growth were composed of varying percentages of cobalt dopant, allowing us to deposit films with varying cobalt concentrations.

A KrF excimer laser was used to create a 25 mJ laser beam that was focused down to a 5 mm^2 spot on the target, resulting in a fluence of 0.5 J/cm^2. The targets were ablated for 60 minutes for all growths and ablated for 5 minutes in vacuum prior to growth, to remove any impurities and loose material on their surfaces, enhancing the purity and quality of the deposited material. As in un-doped TiO_2 multiple substrates were loaded for each growth allowing deposition onto sapphire, silicon and $SrTiO_3$ substrates simultaneously. A summary of the growth conditions used to create the Co:TiO_2 samples is shown in table 5.1.

Film Label	Substrate	Target	Growth Pressure	Substrate Temperature	Post growth Annealing
PLD43_1	sapphire	Co(3%):TiO_2	10 mTorr	550 °C	none
PLD43_2	sapphire	Co(3%):TiO_2	0.2 mTorr	700 °C	none
PLD43_3	sapphire	Co(3%):TiO_2	10 mTorr	550 °C	700 °C, 1hr
PLD43_4	sapphire	wet-Co(3%):TiO_2	0.2 mTorr	700 °C	none
PLD43_5	sapphire	Co(6%):TiO_2	0.2 mTorr	700 °C	700 °C, 1hr
PLD43_6	sapphire	Co(12%):TiO_2	0.2 mTorr	700 °C	700 °C, 1hr
PLD43_7	sapphire	Co(3%):TiO_2	0.2 mTorr	700 °C	700 °C, 1hr
PLD45_1	$SrTiO_3$	Co(3%):TiO_2	10 mTorr	550 °C	none
PLD45_2	$SrTiO_3$	Co(3%):TiO_2	0.2 mTorr	700 °C	none
PLD45_3	$SrTiO_3$	wet-Co(3%):TiO_2	0.2 mTorr	700 °C	none
PLD45_4	$SrTiO_3$	Co(6%):TiO_2	0.2 mTorr	700 °C	700 °C, 1hr
PLD45_5	$SrTiO_3$	Co(12%):TiO_2	0.2 mTorr	700 °C	700 °C, 1hr
PLD45_6	$SrTiO_3$	Co(3%):TiO_2	0.2 mTorr	700 °C	700 °C, 1hr
PLD44_1	silicon	Co(3%):TiO_2	10 mTorr	550 °C	none
PLD44_2	silicon	Co(3%):TiO_2	10 mTorr	550 °C	700 °C, 1hr
PLD44_3	silicon	wet-Co(3%):TiO_2	0.2 mTorr	700 °C	none
PLD44_4	silicon	Co(6%):TiO_2	0.2 mTorr	700 °C	700 °C, 1hr
PLD44_5	silicon	Co(12%):TiO_2	0.2 mTorr	700 °C	700 °C, 1hr
PLD44_6	silicon	Co(3%):TiO_2	0.2 mTorr	700 °C	700 °C, 1hr
PLD46_1	rutile	Co(3%):TiO_2	0.2 mTorr	700 °C	none

Table 5.1: Summary of growth parameters for Co:TiO_2 samples.

5.2 Structural characterisation

5.2.1 Microscope images

The majority of the sample surfaces were smooth to the resolution of the microscope, although rough films were observed on a few samples, namely PLD45_1, PLD43_1, PLD43_2 and PLD43_3, with the last two (sapphire) samples also showing signs of film peeling. All of the samples also had varying

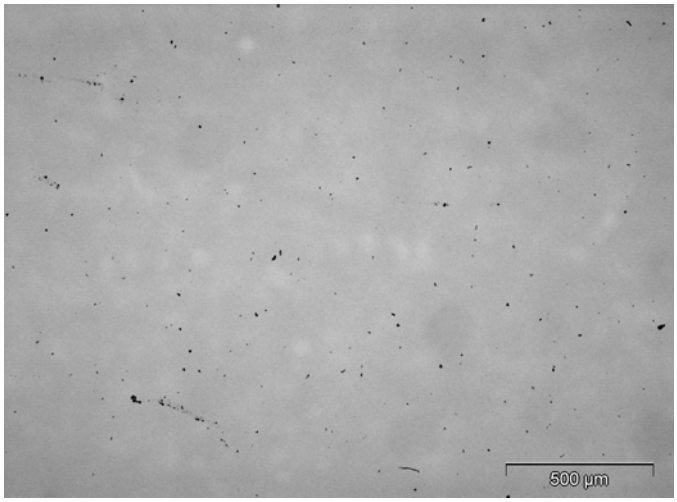

Figure 5.1: Microscope image of the sapphire sample PLD43_5 at 50 times magnification. The unfocused image in the background is the surface of a metal plate on which the transparent sample was sitting.

amount of debris on their surfaces, with a fairly typical amount of debris being shown in a magnified image of a sapphire sample in figure 5.1. The debris is thought to originate from the cleaning of the samples after growth, where the silver paste on the reverse side of the substrates is scraped off with a razor that may result in contamination of the sample surface.

5.2.2 Scanning electron microscope images

Scanning electron microscopy of three Co:TiO_3 samples was performed using the LEO440 at Industrial Research Limited. Excluding small amounts of debris, the samples were found to be smooth up to 2000 times magnification (figure 5.2).

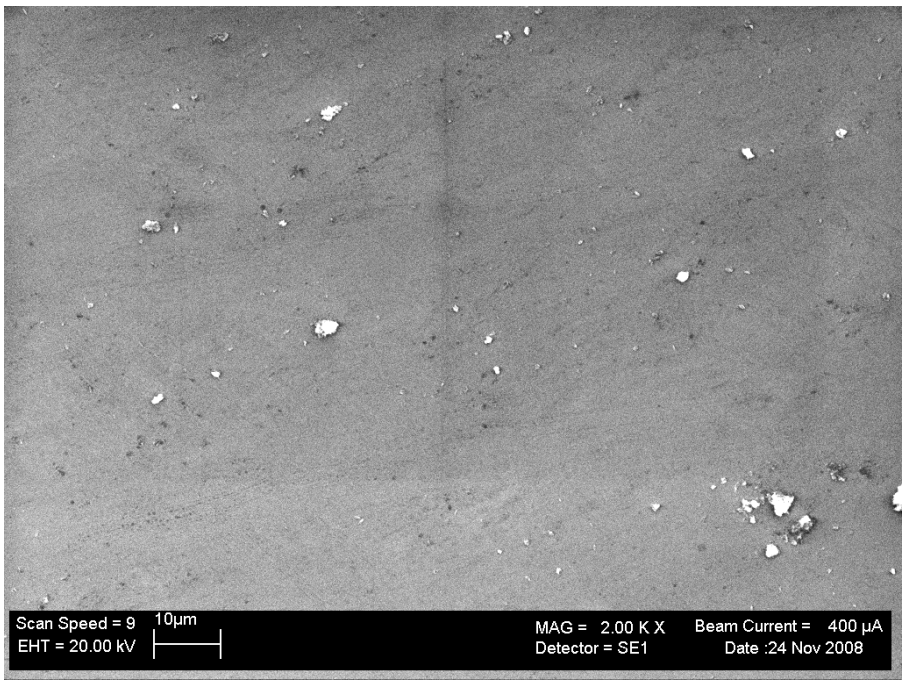

Figure 5.2: SEM image of a Co:TiO_2 film deposited on silicon. This sample had one of the highest concentration of debris of all the samples when viewed under the microscope.

Higher magnification images of the samples were hard to obtain due to the semiconducting nature of the films, which made focusing difficult.

5.2.3 X-ray diffraction

XRD θ-2θ scans were performed on the samples to determine the crystal orientation and grazing incidence scans were performed to detect any polycrystalline phases and unorientated impurity peaks.

The samples grown on sapphire substrates were highly aligned single crystals. They all exhibited the (200) rutile phase (figure 5.3) and had rocking curves of ~0.1°. As in the un-doped TiO_2 samples, we observed the amount of strain to decrease with increasing growth temperature. The shift of the rutile peak for samples grown at 550 °C, 550 °C with annealing, 700 °C and 700 °C with annealing were found to be 0.56°, 0.42°, 0.32° and 0.32° respectively. Grazing incidence was performed on the 12 % cobalt sample and no impurity peaks were found.

The samples grown on $SrTiO_3$ substrates were all found to posses the anatase crystal structure in the (004) orientation (figure 5.4). This was the result we were expecting as the anatase phase has only a 3 % lattice mismatch with the $SrTiO_3$ substrate. The samples were well oriented, with rocking curves around

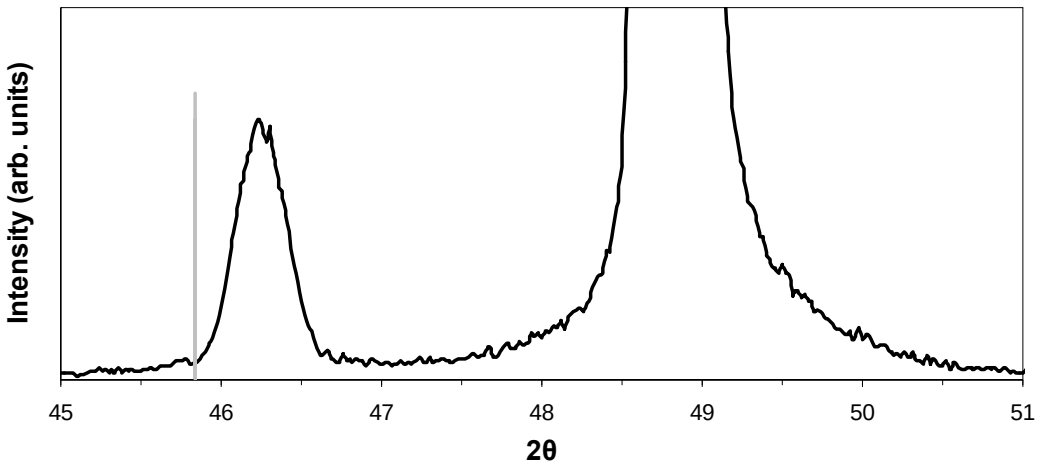

Figure 5.3: X-ray diffraction data from the sapphire sample, PLD43_3 showing a strained (200) rutile peak. The expected position of the rutile (200) peak is shown by the grey line.

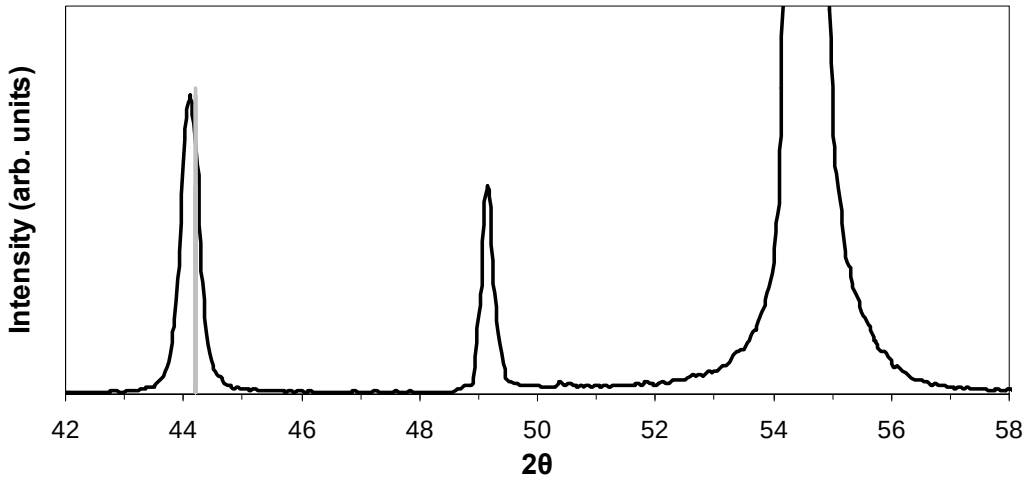

Figure 5.4: X-ray diffraction data from the $SrTiO_3$ sample, PLD45_2 showing a (400) anatase peak. The expected position of the anatase (400) peak is shown by the grey line.

0.8^o. Grazing incidence was performed on PLD45_5 and PLD45_6 (12 % and 3 % cobalt samples, respectively) and two small peaks were observed in both scans. The peaks were unable to be identified but were of similar intensity on both scans which suggests they were not related to any cobalt impurities in the samples as the peaks would be expected to be larger on PLD45_5 due to the higher concentration of cobalt.

The films grown on silicon substrates were found to be polycrystalline, this is unsurprising as silicon is mismatched to the rutile and anatase lattice planes by 18 and 43 %, respectively. The polycrystalline phases where all identified as rutile TiO_2. A grazing incidence scan of the 12 % cobalt sample (PLD44_5) showed a very low intensity $CoTiO_3$ impurity peak. While the presence of cobalt based impurities is disconcerting due to its possible affect on magnetic measurements,

the intensity of the peak is less than 0.5 % of the main rutile peak, in addition the impurity phase $CoTiO_3$ is antiferromagnetic and should not have a noticeable effect on the magnetic measurements shown later in this chapter.

SEM images of the $Co:TiO_2$ samples were not able to be resolved at high enough magnifications to get an indication of the grain size, hence for these samples we used Scherrer's formula,

$$D = \frac{K\lambda}{\beta \cos\theta} \tag{5.1}$$

Where D is the average dimension of the grains, K is a constant between 0.89 and 1 (usually assumed to be 1), λ is the wavelength of the radiation, β is the FWHM of the film peak in radians and θ is the angle at which the peak is located. The FWHM of the peaks on sapphire and $SrTiO_3$ substrates were 0.3^o to 0.4^o which corresponds to grain sizes of ~25 to 35 nm, similar to the grain sizes estimated from SEM images of un-doped TiO_2 films.

5.2.4 Rutherford backscattering spectroscopy

Rutherford backscattering measurements performed by Dr. John Kennedy were used to approximate the film thickness and stoichiometry. Three samples doped with varying concentrations of cobalt were analysed. The estimations of the cobalt concentrations were 2, 6 and 8 % for samples grown using 3, 6 and 12 % targets, respectively. It is difficult to estimate the cobalt concentration in the films from RBS data due to the close proximity of the cobalt and titanium peaks in the RBS

spectrum (figure 5.5). Although accurate values for the cobalt concentrations are difficult to obtain from the data, we were able to verify that the cobalt concentration in the samples was roughly the same as the targets used to grow them.

The thicknesses of the film grown using the Co(3%):TiO_2 target was found to be ~60 nm and the films grown using the Co(6%):TiO_2 and Co(12%):TiO_2 targets were found to be ~85 nm thick. Because the films were all deposited under similar conditions we would expect them to all be of similar thickness, hence the thickness of all Co:TiO_2 films was assumed to be ~70 nm in this work. Although this estimation was used, it was possible that the two targets with higher cobalt concentration may have been less dense, which could have resulted in the deposition of a thicker film. The thickness of the films is non-trivial, as the volume of the films is used to characterise magnetic and resistive properties of the films later in this chapter. However, due to the number of films produced it was impractical to obtain RBS measurements for all of them.

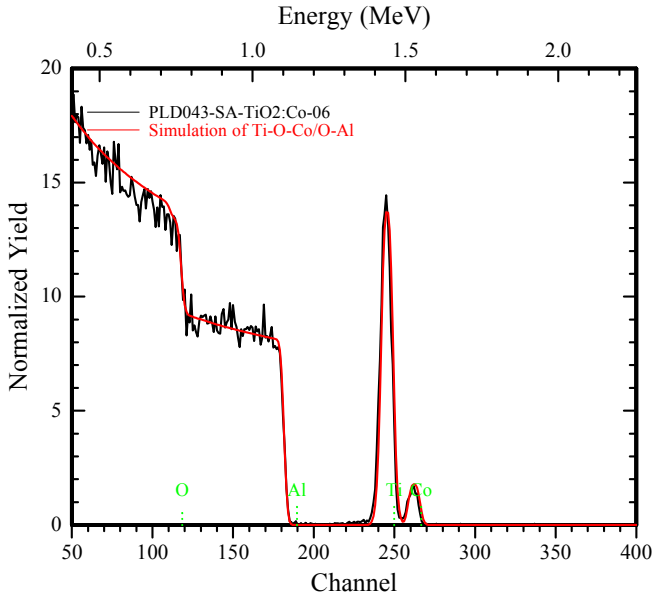

Figure 5.5: RBS measurements of the sapphire sample PLD43_6, showing the close proximity of the titanium and cobalt peaks.

5.3 Optical transmission

Optical transmission measurements were performed on the sapphire samples grown at 700 ^{o}C with post growth annealing on the Cary50 at Industrial Research Limited. Figure 5.6 shows the transmission spectra for three samples with varying degrees of cobalt concentration. The films were transparent in the visible region with optical gaps greater than 3 eV. The spectra shown have not had the sapphire transmission removed as this would result in a misrepresentation of the true transmission due to reflections from the film-substrate interface, which cannot be accounted for by using a blank sapphire substrate as a reference scan. The true

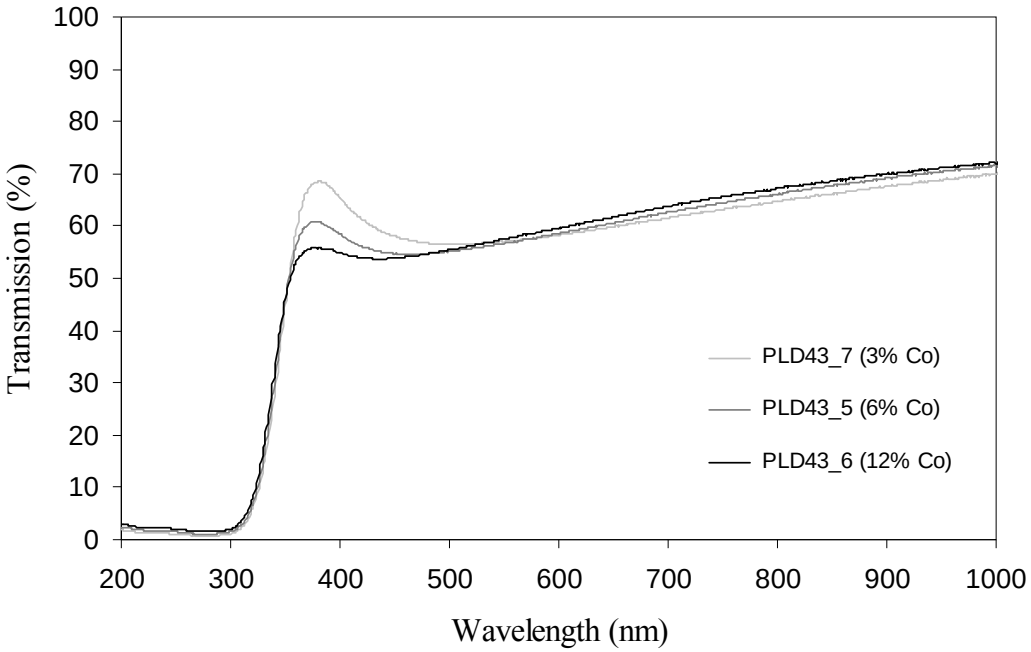

Figure 5.6: Optical transmission of Co:TiO_2 films deposited on sapphire, with varying cobalt concentrations.

transmission of the films from 400 to 1000 nm is around ~15 % higher than shown in figure 5.6.

An increase in absorption over the 350 to 500 nm region is observed for increasing cobalt concentration, which is possible caused by a band edge state in cobalt. To study this effect in further detail, transmittance and reflectance data will need to be collected. Below ~340 nm the films do not transmit and the spectra above ~500 nm is dominated by thin film effects.

The absorption edges of the samples are ~ 345 to 350 nm and upon closer inspection, we can see a small blue shift in the absorption edge for increasing cobalt concentration (figure 5.7). This shift may indicate the influence of the

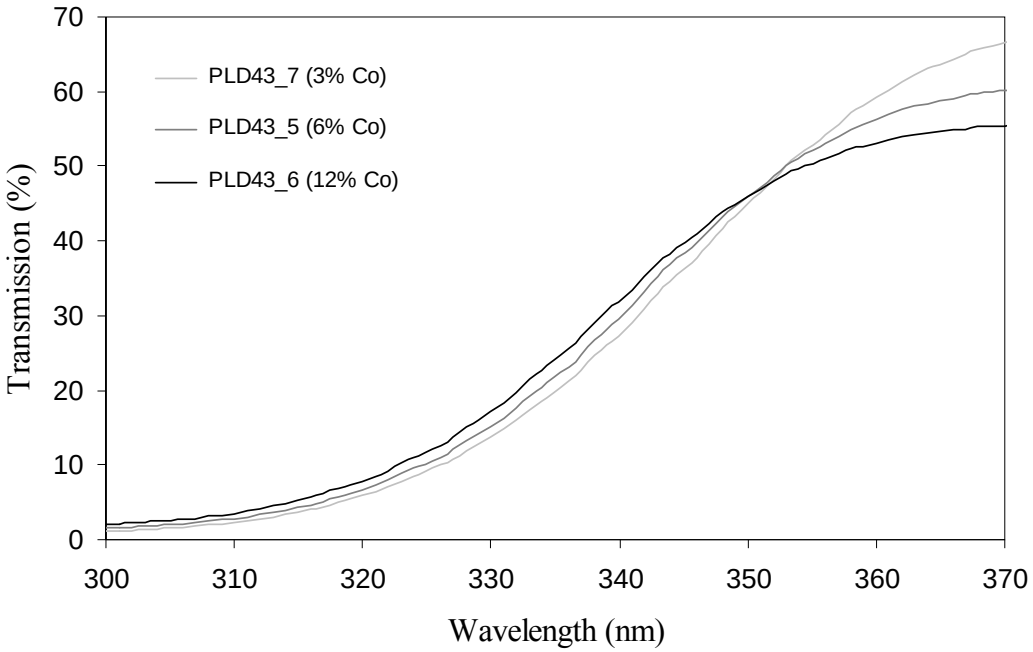

Figure 5.7: Enlarged view of the absorption region.

incorporated cobalt on the electronic states. These kinds of shifts have been observed in dilute magnetic semiconductor systems before [48,49].

Fitting our data with Fresnel's equations and assuming the refractive index, n, of bulk rutile, which is 2.7. We found that a film thickness of 70 nm gave the best fit to the data, in good agreement with the thicknesses calculated from RBS measurements.

5.4 Resistivity measurements

Electrical resistivity measurements were performed on the two sapphire samples, PLD43_7 (3 % Co) and PLD43_6 (12 % Co) and are shown in Figure 5.8. The electrical resistivity, ρ, showed activated behaviour that was fitted to,

$$\rho = \rho_0 e^{\frac{\Delta E}{k_B T}} \tag{5.2}$$

where ρ_0 is a constant, k_B is Boltzmann's constant, and T is the temperature. We found the activation energies, ΔE, to be 79 meV for the 3 % cobalt sample and 67 meV for the 12 % cobalt sample.

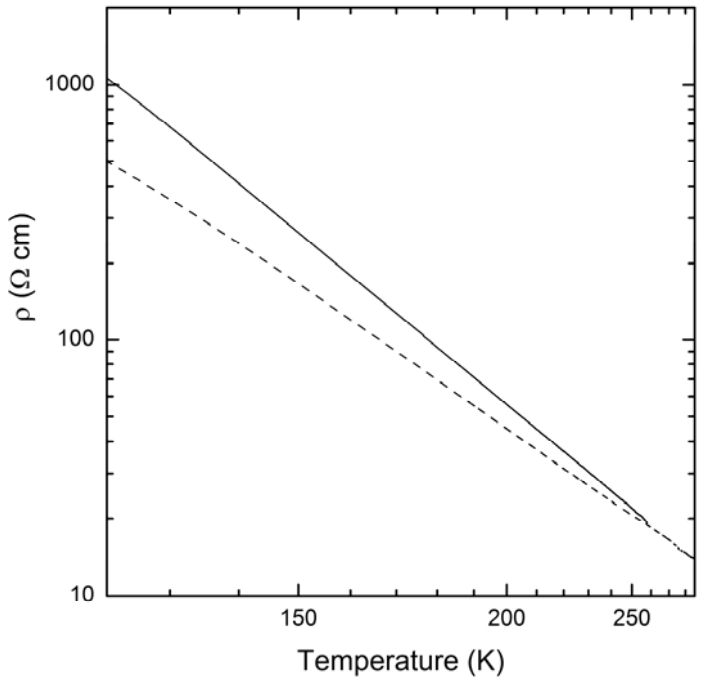

Figure 5.8: Plot of the resistivity data against temperature on a 1/T scale for Co:TiO_2 films on sapphire with 3 % Co (solid curve) and 12 % Co (dashed curve).

The room temperature resistivity and ΔE are within the range of values reported in the literature for Co:TiO_2 films made using similar growth conditions [50,51]. The high resistivities observed in our films suggest that Co:TiO_2 may be difficult to incorporate into commercial spintronics devices. However, the high resistivities are due to the difficulty in controlling the carrier concentration during deposition and recent research has shown that high n-type conductivities can be achieved by using lower oxygen gas pressures during growth to induce oxygen vacancies [51,52], or actively doping with Nb [53]. Researchers using these methods have found it is possible to reduce the resistivity below 1 Ωcm down to low temperatures, while still maintaining ferromagnetic behaviour at room temperature.

5.5 Magnetic measurements

Magnetic measurements of the samples were recorded in a temperature range of 5 to 400 K and in magnetic fields up to 6 T using the SQUID magnetometer at Industrial Research Limited. Field loops up to 4 Tesla were performed at 10 K on all of the sapphire samples and a selection of silicon and $SrTiO_3$ samples.

The relationship between the magnetic properties of the films and the substrates they were grown on varied, but in general the saturation moment (m_s) was highest for the films deposited on silicon and lowest for films deposited on $SrTiO_3$ substrates. The maximum m_s found on each of the different substrates was

7.0, 5.8 and 0.48 μ_B/Co for a silicon, sapphire and $SrTiO_3$ sample, respectively. Figure 5.9 shows a field loop of the film with an m_s of 7.0 μ_B/Co grown on silicon and an enlargement showing the coercive field.

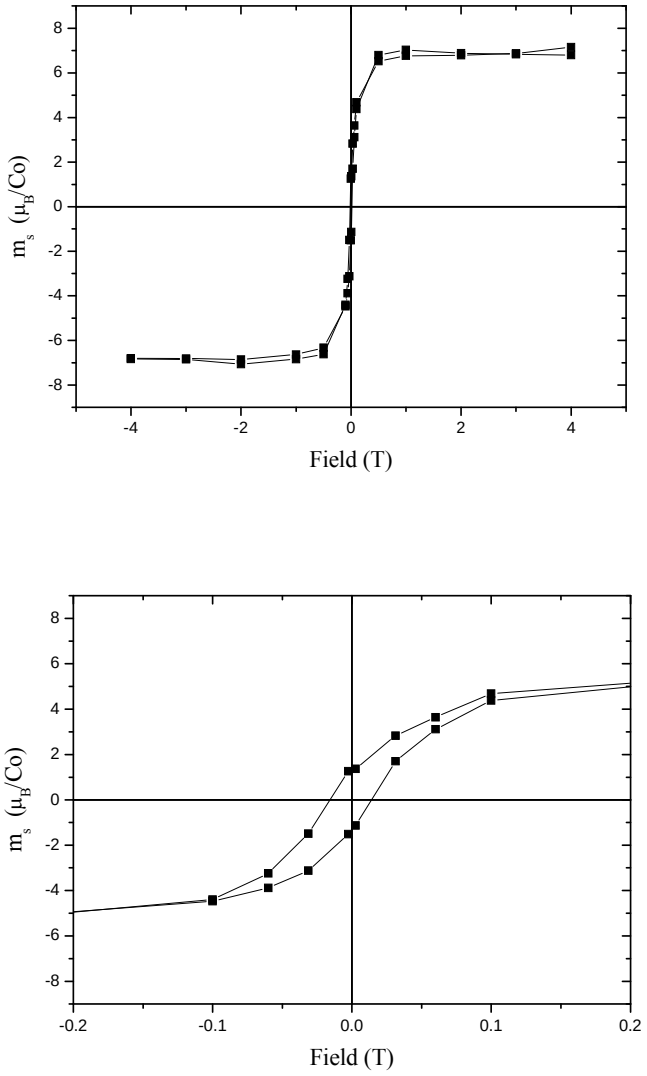

Figure 5.9: Field loop of a sample grown on silicon (PLD44_2) showing a magnetic saturation of 7.0 μ_B/Co. The bottom figure shows an expanded view of the coercive field.

The values we obtained for m_s are higher than what is usually reported in the literature with most researchers finding m_s values from 0.1 μ_B/Co up to the value for cobalt metal, 1.7 μ_B/Co [54]. Most Co:TiO_2 research is however, carried out with anatase films, even though rutile is often observed to have a higher moment than anatase films produced in similar conditions [14,55]. While not common, there have been other studies on Co:TiO_2 with reported moments of 3 to 7 μ_B/Co [56,57]. Similarly large values have also been reported for Co:ZnO which is closely related to Co:TiO_2 [58,59]. The calculation of m_s values is dependant on the calculated film thickness and cobalt concentration in the samples. Both of these values have been estimated from the RBS data of three samples; the thickness and cobalt concentrations of the rest of the samples were estimated based on these measurements. This could have introduced errors in the assumed film thickness and cobalt concentration of the samples, resulting in overestimations of m_s. It may however be that our values are more accurate than we presume. The charge of substituted cobalt has been determined to be Co^{2+} by x-ray photoelectron spectroscopy and x-ray absorption spectroscopy by several different groups [10,54]. However, the spin configuration of incorporated cobalt is not so well defined, with different groups supporting claims it is in the low spin state ($3d^7$, s = ½, 1 μ_B/Co spin moment) or the high spin state ($3d^7$, s = ½, 3 μ_B/Co spin moment). If the magnetism in our samples originates from cobalt, our high values suggest that the incorporated cobalt is in the high spin

configuration. It is also possible a cobalt oxide with a high moment could explain the high saturation moments, but no known cobalt oxides are ferromagnetic, CoO, Co_2O_3, Co_3O_4 and $CoTiO_3$ are all antiferromagnetic below room temperature [60].

Oxygen vacancies in the TiO_2 lattice stabilised by substituted cobalt atoms play a key role in several models that account for the ferromagnetism observed in Co:TiO_2. Samples grown with 3 % cobalt concentration were prepared with two different combinations of temperature and oxygen pressure to create different concentrations of oxygen vacancies in the films, 10 mTorr at 550 ^oC and 0.2 mTorr at 700 ^oC (see section 5.1). Annealing post growth at 700 ^oC was also performed on some of the growths to remove more oxygen from the samples. The high temperature and low pressure was found to increase the m_s at 10 K for sapphire samples, highlighting the role of oxygen vacancies (figure 5.10). The effect of both annealing [55] and lower growth pressures [61] on increasing the m_s of Co:TiO_2 sapphire samples has been observed independently in other reports. However, the role of oxygen deficient environments in increasing the m_s is controversial, where one particular group reported the increase in magnetism was due to cobalt nanoparticles whose formation was assisted by an oxygen deficient growth atmosphere [61], while another group thought it was the oxygen vacancies created from annealing that played the important role in increasing the magnetic moment of the films [55]. Recently it has been shown that ferromagnetism at room temperature can be achieved in un-doped TiO_2 films [17,18], with significantly higher magnetic moments being observed in films grown in oxygen

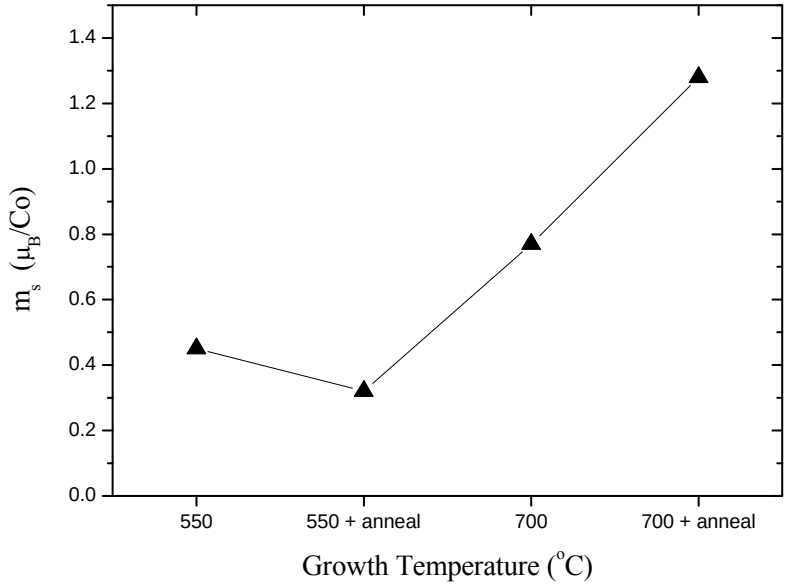

Figure 5.10: Relationship between growth temperature (and annealing) and the resulting m_s at 10 K for sapphire samples with 3 % cobalt concentration.

deficient environments [17]. As no cobalt is present, these reports give strong evidence that it is the oxygen vacancies rather than cobalt clusters which are responsible for the observed increase in the magnetic moment. Strangely the reverse was found to be true for our samples grown on silicon, which showed reduced m_s values when prepared at higher temperatures and lower pressures. However, the cleanliness of some of the silicon substrates has been questioned due to colourful patterns found on some of their surfaces, indicating that an impurity (perhaps some oil off a finger) was present on the substrate surfaces prior to growth.

Field loops of several samples grown on each of the substrates were

performed at 300 K, all of which showed ferromagnetic behaviour, indicating the Curie temperature of the samples is above room temperature. Although the samples were still ferromagnetic at 300 K, they did show decreases from 5 to 20 % in the saturation moment and decreases in remnant magnetisation of ~45 % in comparison to the 10 K field loops. A more detailed study was performed on the sample PLD43_04 which showed the highest m_s of the sapphire samples at 10 K.

Field loops of PLD43_4 were performed at temperatures ranging from 5 to 370 K, the effect of temperature on m_s and remnant magnetisation are shown in figures 5.11 and 5.12 respectively. The origin of the high m_s of the sample observed at low temperatures is unknown. It cannot have originated from unordered cobalt, as both diamagnetic and paramagnetic contributions are removed from the data. It could be that the cobalt is not randomly distributed in the film, instead forming 'pockets' of cobalt thought the film. This could lead to two ordering temperatures, one at high temperature for the neighbouring cobalt atoms and the other at ~20 K for the pockets of cobalt. The sharp increase could also be attributed to Co_2TiO_4 which is ferrimagnetic below 55 K, however no peaks of this impurity were found in the XRD data of the samples. After this initial decrease, the m_s remains relatively constant from 20 – 250 K with a noticeable decrease in the magnetisation after 250 K. The remnance of the sample showed similar behaviour. A linear extrapolation of $m_s(T)$ and remnance(T) showed the Curie temperature of the sample to be approximately ~600 K, a value which is commonly reported in the literature, although it is often disputed.

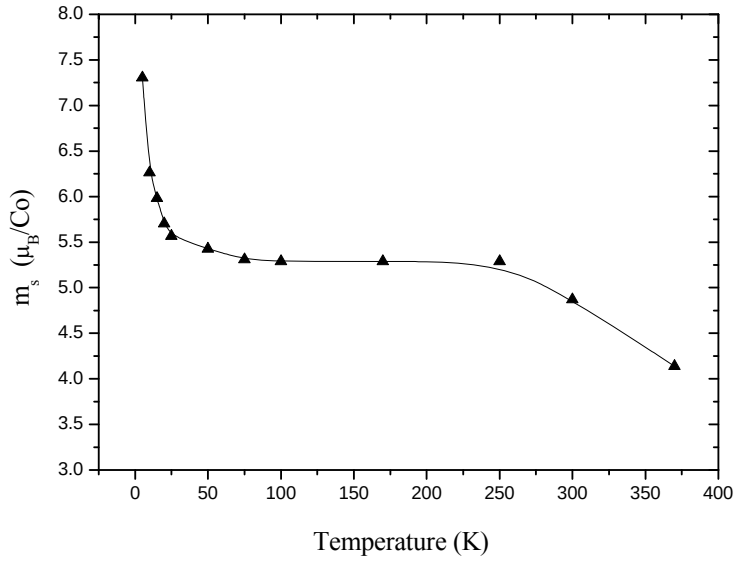

Figure 5.11: Saturation magnetisation as a function of temperature for a 3 % cobalt film on sapphire (PLD43_4). The line shown is a guide for the eye only.

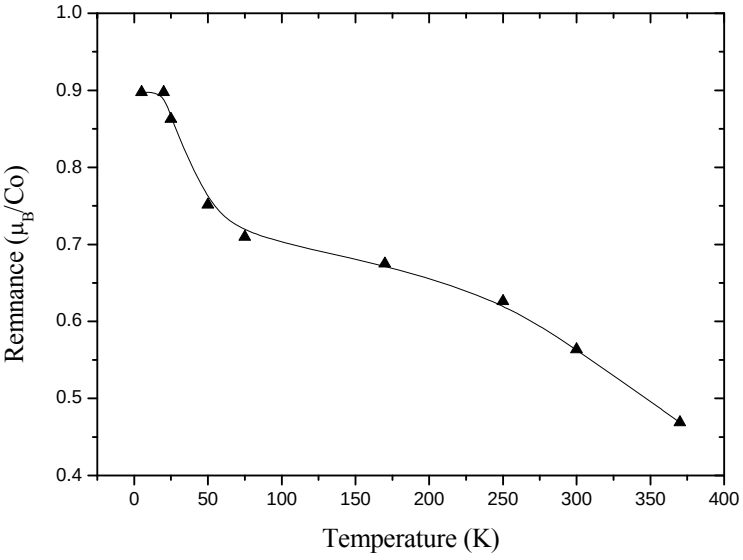

Figure 5.12: Remnant magnetisation as a function of temperature for a 3 % cobalt film on sapphire (PLD43_4). The line shown is a guide for the eye only.

Co:TiO_2 samples with cobalt concentrations of 3, 6 and 12 % were deposited on sapphire and $SrTiO_3$ substrates, these films were deposited at 700 ^oC in 0.2 mTorr and were annealed at 700 ^oC in vacuum immediately after growth. In our samples the increased cobalt concentration resulted in increases in the moment per unit volume but the m_s per cobalt atom decreased (figure 5.13). If the magnetism in our samples originates from cobalt nanoclusters then the m_s per cobalt atom would be expected to remain fairly constant for increasing concentrations of cobalt, which is not the case. With a Curie temperature of ~1400 K cobalt clusters would be expected to show ferromagnetic behaviour well above room temperature. The energy required to decouple the moments of neighbouring

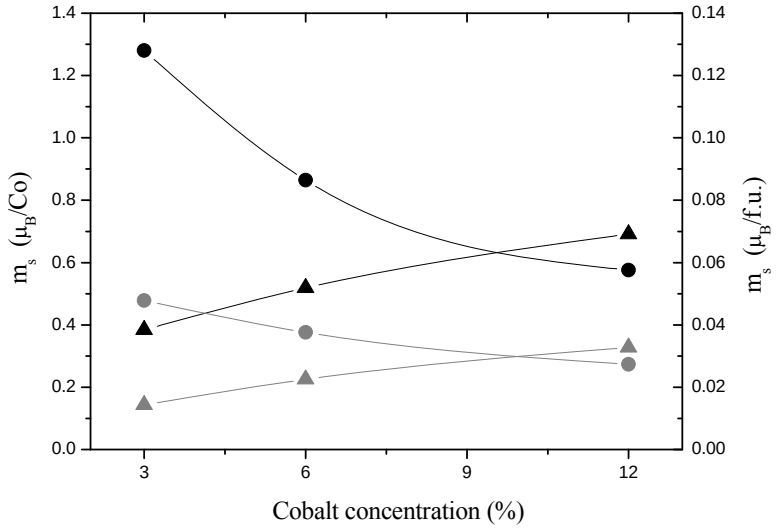

Figure 5.13: The black lines show the m_s of sapphire samples and the grey lines show the m_s of the films deposited on $SrTiO_3$ substrates. The triangles and circles show the m_s in units of μ_B/f.u. and μ_B/Co respectively.

cobalt atoms is high so in the absence of an applied field at 300 K the moments of neighbouring cobalt atoms would be expected to remain aligned. However, coupling between neighbouring cobalt clusters is much weaker due to the distance of the coupling. Hence the energy required to decouple the moments (the crystalline anisotropy energy) of the crystallites is much lower than the Curie temperature of cobalt and is proportional to the size of the clusters. If the clusters were small, we would expect them to be superparamagnetic at room temperature but we clearly see remnance at 300 K. Large clusters would have a higher crystalline anisotropy energy and could account for the observed remnance at 300 K. However if there were large cobalt clusters (greater than ~4 nm) present in the films we would expect them to have been detected using XRD measurements, which was not the case. This suggests that cobalt clusters are not responsible for the observed ferromagnetism in our films.

5.6 Summary

We have deposited Co:TiO_2 thin films on sapphire, silicon and $SrTiO_3$ substrates. We found the substrates to have a large effect on the adopted crystal structure of the film. We deposited highly orientated (200) rutile, polycrystalline rutile and (004) anatase on sapphire, silicon and $SrTiO_3$ substrates, respectively. No impurities were found on the sapphire or $SrTiO_3$ samples, although a small $CoTiO_3$ impurity peak was found on a silicon sample. The films were optically

transparent in the visible region with band gaps greater than 3 eV. Ferromagnetic behaviour believed to be intrinsic was observed in the films up to 300 K, with saturation moments ranging from 0.2 to 7.0 μ_B/Co. A detailed temperature dependant study of the sample PLD43_4, indicated the sample had a Curie temperature of ~600 K, consistent with values commonly reported in the literature.

Chapter 6

Sr_2FeMoO_6

Recently, the half metallic double perovskite Sr_2FeMoO_6 (SFMO) has received attention due to the discovery of large low-field MR at room temperature in sintered polycrystalline pellets. The half-metallicity, large MR and high Curie temperature make SFMO an ideal candidate for spintronic and magnetoresistive devices. Eventual applications of this material rely on the synthesis and characterisation of SFMO thin films. However it has been observed that epitaxially grown films do not exhibit the large MR that is found in polycrystalline samples, which has led researchers to believe the MR arises from spin polarised tunnelling between insulating grain boundaries. Unfortunately attempts to introduce tunnelling barriers in SFMO thin films has failed to achieve the large MR values observed in the polycrystalline bulk samples [62].

We deposited SFMO films on a selection of substrates and varied the substrate temperature during growth in an effort to obtain grain boundaries capable of large low field MR at room temperature. In this chapter we describe the method and parameters used for deposition and report the results from the structural and magnetic characterisation of the samples.

6.1 Pulsed laser deposition

The SFMO samples were produced by the PLD method. A KrF excimer laser was used to produce a 60 mJ laser beam which was passed through a quartz lens and focused down to a 3.5 mm^2 spot on the SFMO target, creating a laser fluence of around 1.8 J/cm^2 during growth. The target was pre-ablated for 5 minutes prior to all growths to remove any impurities on the surface. The growths were performed for a 60 minute duration with multiple substrates being loaded onto the substrate holder simultaneously, allowing near identical depositions to be performed on a selection of substrates. The HV chamber was backfilled with oxygen creating a pressure of 0.2 mTorr for the growths. There was however, one deposition that was performed in vacuum at a pressure of 1×10^{-5} Torr. These low pressures were used to reduce the formation of unwanted impurity phases that tend to form at higher pressures [63]. The substrate temperature was varied for different growths, but in all cases the temperature of the substrates was ramped down at 10 ^oC per minute after deposition to prevent thermal shock and cracking of the film. A summary of the SFMO samples produced is shown in table 6.1.

Film Label	Substrate	Growth Pressure	Substrate Temperature
PLD48_1	$SrTiO_3$	0.2 mTorr	800 ^oC
PLD48_2	$SrTiO_3$	0.2 mTorr	750 ^oC
PLD48_3	$SrTiO_3$	0.2 mTorr	850 ^oC
PLD48_4	$SrTiO_3$	0.2 mTorr	650 ^oC
PLD48_5	$SrTiO_3$	1E-5 Torr	800 ^oC
PLD59_1	sapphire	0.2 mTorr	750 ^oC
PLD59_2	sapphire	0.2 mTorr	850 ^oC
PLD59_3	sapphire	0.2 mTorr	650 ^oC
PLD59_4	sapphire	1E-5 Torr	800 ^oC
PLD60_1	silicon	0.2 mTorr	750 ^oC
PLD60_2	silicon	0.2 mTorr	850 ^oC
PLD60_3	silicon	0.2 mTorr	650 ^oC
PLD60_4	silicon	1E-5 Torr	800 ^oC
PLD66_1	glassy carbon	1E-5 Torr	800 ^oC

Table 6.1: Summary of the temperature, pressure and substrates used to deposit the SFMO thin films.

6.2 Structural characterisation

6.2.1 Microscope images

The Olympus BX60M microscope was used to take high magnification images of the samples. The samples grown at 850 ^oC were noticeably rough under the microscope at 200 times magnification, while the films grown at lower temperatures were generally smooth. There was also some square shaped structures approximately 1 μm in size visible on PLD48_01 (figure 6.1). Almost identical microstructures were found by both D. Sánchez *et al*. [21] and J. Santiso *et al*. [64]. However, the two groups deduced different compositions for the microstructure claiming they were $SrMoO_4$ and Fe_3O_4, respectively.

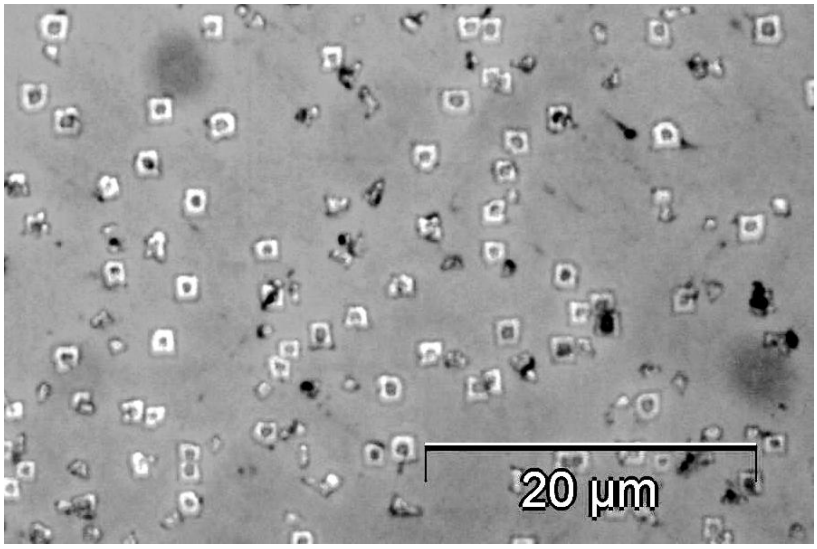

Figure 6.1: Microscope image of the sample PLD48_01 showing square microstructures present in the film deposited on a $SrTiO_3$ substrate.

6.2.2 Scanning electron microscope images

High magnification images of the samples PLD48_3 and PLD60_2 were taken using the LEO 440 SEM located at Industrial Research Limited to gain information on the morphology of the films. The grains are thought to play a key role in the large MR seen at room temperature in SFMO. The images showed that the grain morphologies of the samples grown on different substrates differed significantly. The silicon sample, PLD60_2, showed grains that were closely packed together throughout the film and appeared spherical in shape (figure 6.2). The sample PLD48_3, grown on $SrTiO_3$ had a very different morphology to PLD60_2, with well-connected grains that did not take on any particular shape (figure 6.2).

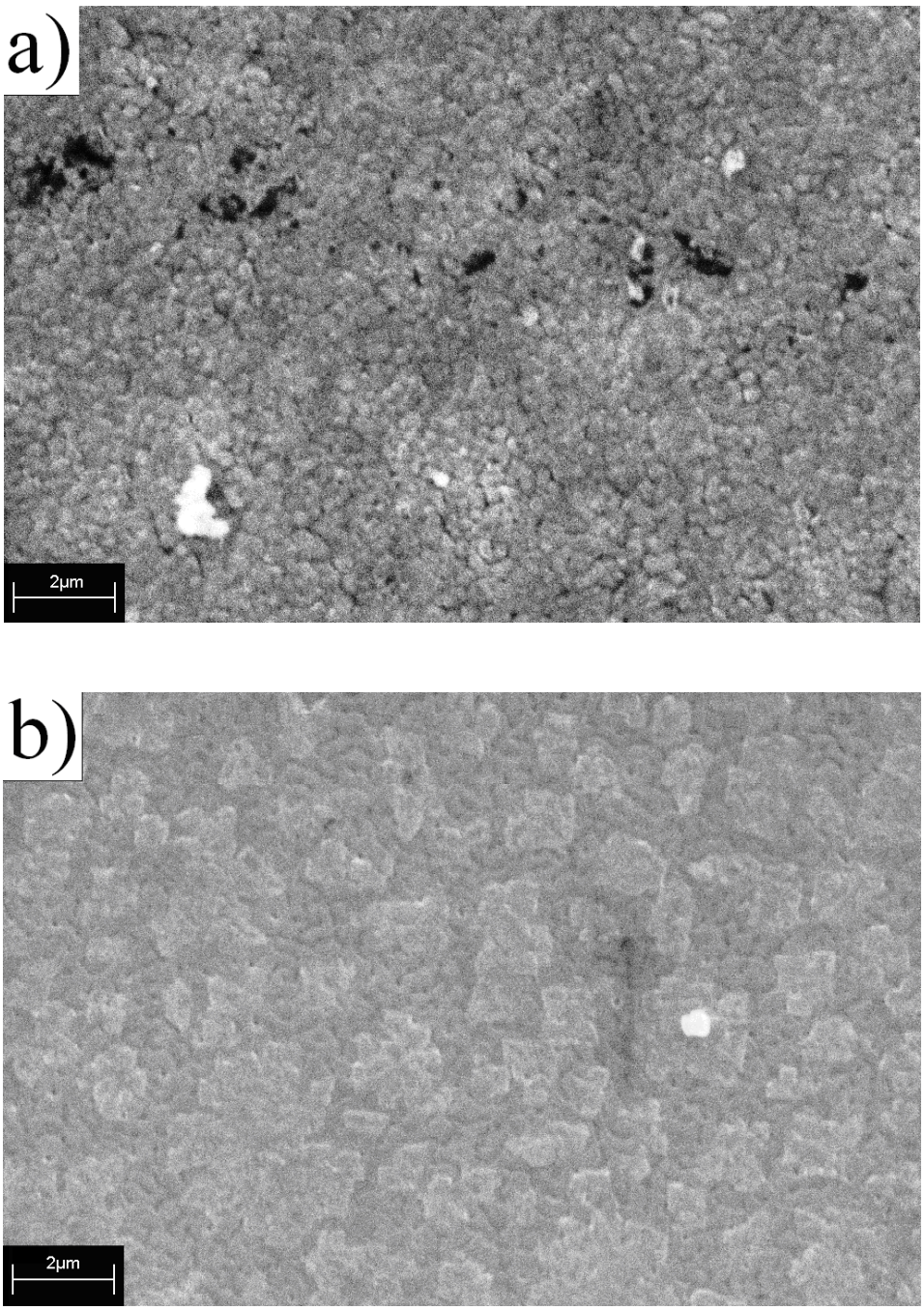

Figure 6.2: SEM images of (a) PLD60_02 deposited on silicon and (b) PLD48_03 grown on $SrTiO_3$.

6.2.3 X-ray diffraction

X-ray diffraction measurements of the films deposited on $SrTiO_3$ substrates revealed a dominant peak at ~53.4^o, which was identified to be the (004) reflection of SFMO shifted by ~-0.5^o. This peak was highly oriented on all the $SrTiO_3$ samples with rocking curves around ~0.3^o, indicating the depositions were epitaxial. The films were likely to have tetragonal distortion from the cubic structure, but it is difficult to verify, as the difference in the expected XRD peaks is very small. These films also showed a weak (220) SFMO peak at ~37.4^o. Grazing incidence of the films revealed the presence of polycrystalline $SrMoO_4$, with the tetragonal structure.

The samples on sapphire substrates were polycrystalline SFMO with the exception of the (311) SFMO peak at 44.0^o which was highly oriented with a rocking curve of ~0.3^o. The impurity phase, $SrMoO_4$ was also found, and was particularly predominant on the sample grown at 850 ^{o}C. The relationship between the formation of this impurity phase and the growth temperature has been seen in the literature [21]. The increase of the $SrMoO_4$ impurity phase at high temperatures may indicate the sample is decomposing, as it is known SFMO decomposes in air at ~400 ^{o}C.

The silicon samples showed some weak polycrystalline SFMO peaks and XRD grazing incidence scans of the samples did not reveal any unorientated impurity phases.

The impurity phase, Fe_3O_4 that is known to be ferromagnetic, was not found

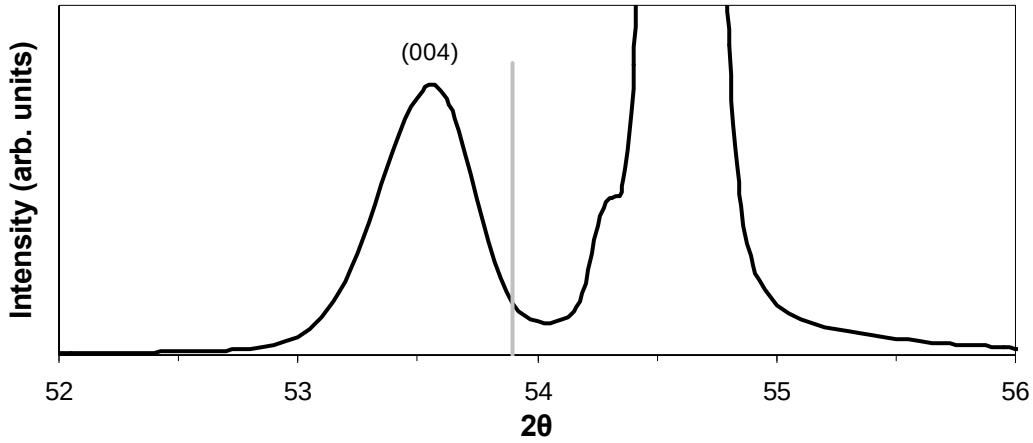

Figure 6.3: XRD 2θ scan of PLD48_3, grown on $SrTiO_3$, showing the shifted (004) SFMO peak. The expected position of the peak is shown by the grey line. The large peak at 54.6^{o} is from the substrate.

in the XRD grazing incidence scans of any of the films.

6.2.4 Rutherford backscattering spectroscopy

Rutherford backscattering measurements of two samples, PLD60_02 and PLD66_01 deposited on silicon and glassy carbon, respectively, were performed by Dr. John Kennedy. Due to the amorphous nature of the glassy carbon substrate, the stoichiometry of the sample was able to be accurately measured from the RBS data, showing the film was a stoichiometric match to the target used for growth (Sr_2FeMoO_6). The calculated stoichiometry of the PLD60_02 was slightly different with $Sr_2Fe_1Mo_{1.2}O_{5.6}$, but probably not as accurate due to the silicon substrate peaks overlapping the film peaks in the RBS data. The films were found to be 450 $^{+}$/- 50 nm thick.

6.3 Magnetic response

Field dependant magnetic measurements were performed up to 4 T at 10 and 300 K using the SQUID magnetometer. We found the m_s of the samples to increase with the growth temperature, with maximum values being obtained for samples grown at 850 ^oC, which were just over double the saturation moments obtained for films grown at 650 ^oC (figure 6.4). J. H. Song *et al*. [65] found the same trend and noted that samples prepared above 850 ^oC showed reduced m_s, which they attributed to increased disorder on the Mo and Fe lattice sites (anti-site disorder). Figure 6.5 shows the field loops for SFMO samples grown on sapphire substrates at different growth temperatures.

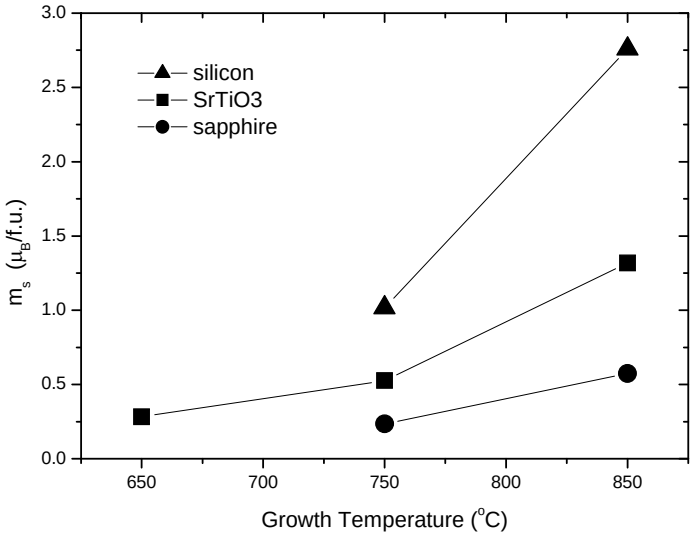

Figure 6.4: The temperature of the substrates during deposition has a large affect on the resulting m_s of the film. Shown here are the m_s of silicon, $SrTiO_3$ and sapphire samples as a function of the growth temperature.

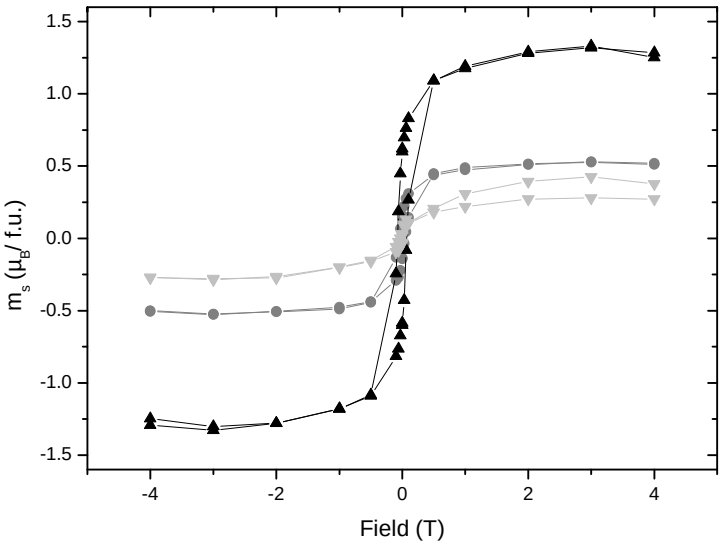

Figure 6.5: Field loops performed at 10 K for SFMO samples grown on sapphire substrates at temperatures of 850 ^{o}C (black triangles), 750 ^{o}C (grey circles) and 650 ^{o}C (light grey triangles).

When comparing the m_s for samples grown on different substrates under the same conditions we see a clear pattern, with silicon having the highest m_s followed by $SrTiO_3$ substrates and with sapphire exhibiting the lowest m_s. Figure 6.6 shows field loops of samples deposited on the three different substrates, at temperatures of 750 ^{o}C and at 850 ^{o}C. Although the m_s changes at the different growth temperatures, we note that the relative magnitude of m_s for the different substrates remains constant. This relationship also held true for the samples deposited at 650 ^{o}C. The maximum saturation moments found for films deposited on silicon, $SrTiO_3$ and sapphire substrates were 2.8, 1.3 and 0.6 μ_B/f.u. respectively. The discrepancy in these observe values and the expected value of

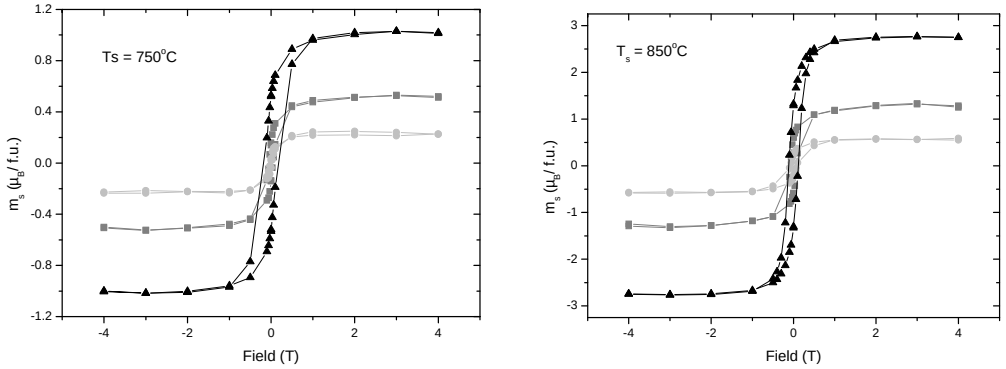

(a) (b)

Figure 6.6: Field loops of SFMO grown on silicon (black triangles), $SrTiO_3$ (grey squares) and sapphire substrates (light grey circles). Films deposited at (a) 750 ^oC and (b) 850 ^oC both show very similar relative m_s magnitudes for the films deposited on different substrates.

4 μ_B/f.u. is commonly attributed to anti-site disorder in the literature [28]. The large moment observed for the silicon samples suggests that they have less anti-site disorder than the oriented samples. It is possible the magnetism arises from nano-crystallites with low anti-site disorder that favour formation on the polycrystalline films.

Field loops performed on a selection of the samples at 300 K showed ferromagnetic behaviour, although a 10 to 20 % reduction in the m_s of the films was observed (figure 6.7). This decrease in m_s is consistent with a Curie temperature of around 450 ^oC, which is commonly reported in the literature [20,22,66]. The decrease in the m_s below the Curie temperature has been attributed to spin-wave dispersion [25]. The effect of the spin-wave dispersion can

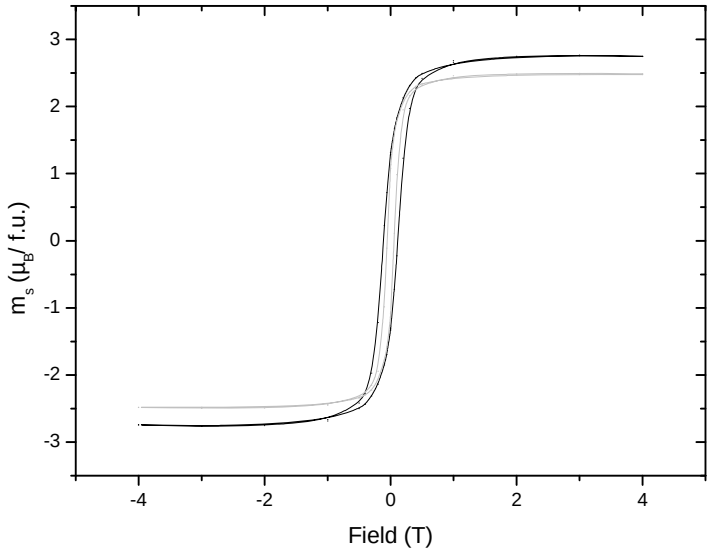

Figure 6.7: Field loops for the sample PLD60_2 grown on silicon performed at 10 K (black line) and 300 K (grey line). This sample showed the highest m_s in our films. The data points have been omitted from this figure for clarity.

be modelled by the equation,

$$m(T) = m_s(1 - a_0 T^n) \tag{6.1}$$

Where, *m(T)* is the spontaneous magnetic moment, m_s is the saturation magnetic moment, T is the temperature and a_o is the spin-wave dispersion.

The coercive field of the samples at 10 K was found to be roughly proportional to their saturation magnetic moments. Measurements of the films deposited on sapphire and $SrTiO_3$ substrates at 300 K showed large decreases of up to 60 % in their coercive fields when compared to measurements performed at 10 K (figures 6.8 and 6.9). The decrease in the coercive field is much larger than the 10 to 20 % decreases observed in the m_s, this is because the coercive field

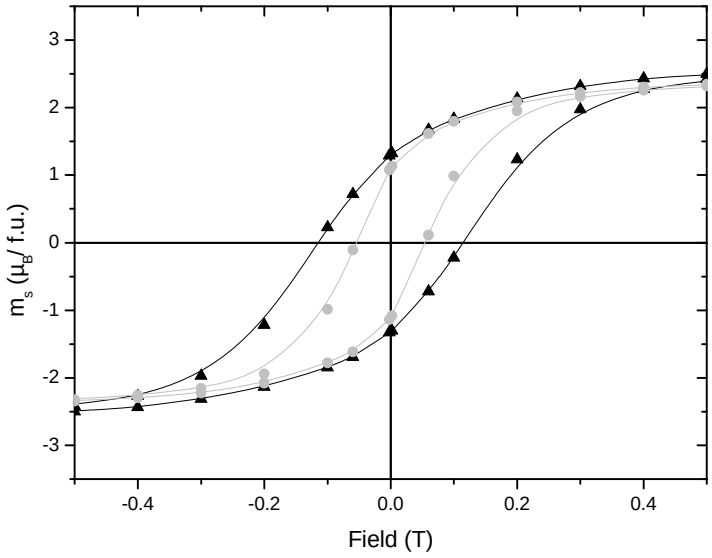

Figure 6.8: Expanded view of the field loops for the sample PLD60_2 grown on silicon performed at 10 K (black triangles) and 300 K (grey circles). This sample showed the highest m_s in our films.

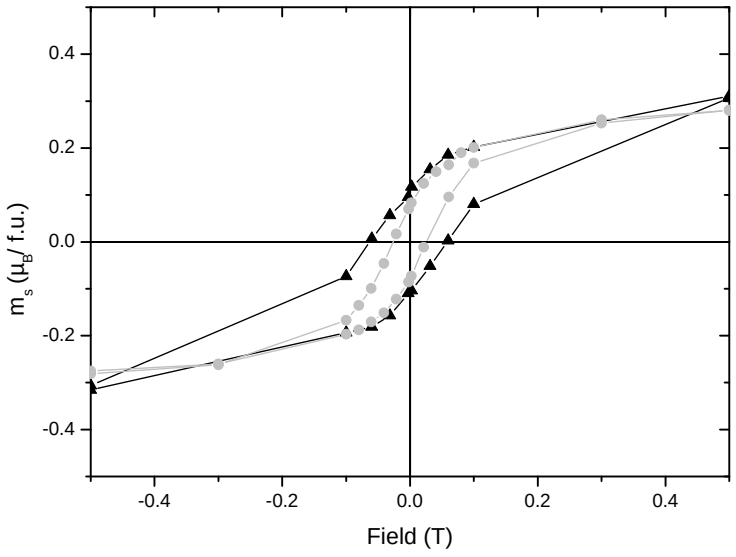

Figure 6.9: Expanded view of the field loops performed at 10 K (black triangles) and 300 K (grey circles) on the $SrTiO_3$ sample, PLD48_1.

arises from domain wall pinning. At room temperature the magnetic field require to 'unpin' or uncouple two magnetic domains is much less than at 10 K, hence the observed decrease in the coercive field at higher temperatures. For practical applications it is desirable to reduce the coercive field by as much as possible.

6.4 Summary

Double perovskite films approximately 450 nm thick were deposited on silicon, sapphire and $SrTiO_3$ substrates. The crystalline quality of the films deposited on $SrTiO_3$ substrates was good with a highly oriented (004) SFMO peak being found in the XRD data while the films deposited on sapphire and silicon were polycrystalline. Grazing incidence scans revealed the presence of a $SrMoO_4$ impurity phase on the samples and it is suspected this impurity phase was the cause of microstructures seen under the microscope on some of the samples. Magnetisation data of the samples showed that increasing the growth temperature from 650 ^oC to 850 ^oC increased the saturation moment of the films by over 200 %. Films deposited on silicon recorded the highest magnetic moments for all growth conditions, with the film deposited at 850 ^oC (PLD60_2) having a saturation moment of 2.8 μ_B/f.u. The films were found to be ferromagnetic up to 300 K, with estimated Curie temperatures ~ 450 K.

Chapter 7

$SrFeO_{3-\delta}$

The transition metal oxides have received much attention lately due to their unusual properties that can be significantly altered by small variations in oxygen content [67]. In particular, $SrFeO_{3-\delta}$ has very interesting magnetic, electric and transport properties that can be substantially altered by synthesising the compound with different oxygen stoichiometries [32,68]. The variation in oxygen content also results in unique crystal structures. In addition $SrFeO_{3-\delta}$ is of interest as it is closely lattice matched to SFMO and may be able to be incorporated in antiferromagnetic-ferromagnetic multilayers with SFMO for practical applications. Although bulk $SrFeO_{3-\delta}$ is often studied, thin films are more desirable, as practical applications will depend on the ability to produce well characterised thin films. It is also easier to vary the oxygen content in thin films due to the higher oxygen diffusion rates during annealing.

We produced $SrFeO_{3-\delta}$ films by PLD and attempted to create films with varying oxygen content by controlling the deposition pressure and subjecting the samples to post growth annealing. The growth and structural characterisation of the resultant films is presented in this chapter.

7.1.1 Film synthesis

7.1.1 Pulsed laser deposition

Deposition of $SrFeO_{3-\delta}$ films was performed using the PLD technique. The KrF excimer laser was used to create a beam with 55 mJ of energy, which was focused down to a 3.5 mm spot on the $SrFeO_{3-\delta}$ target, creating a 1.6 mJ/cm^2 fluence during growth. As with the SFMO growths, the target was ablated for 5 minutes in vacuum prior to all depositions, which were performed over a 60 minute duration. The substrate holder was mounted with multiple substrates for each growth and heated to 700^{o}C prior to and for the duration of the film deposition. The HV chamber was back-filled with oxygen during growth at pressures from 0.2 mTorr up to 80 mTorr to create films with varying oxygen concentrations (table 7.1). Unfortunately due to the gap in the measurable pressures between the Pirani gauge and the Ion gauge, the growth pressure for samples that were deposited in 4 mTorr of oxygen partial pressure were unable to be recorded accurately, but have been assumed to be around 4 mTorr. A single growth was performed on a glassy carbon substrate for the purposes of determining the oxygen content of the film from RBS measurements, as the amorphous nature of the glassy carbon means that no substrate peaks appear in the RBS data making the film peaks easier to analyse. Note that some of the samples have been prepared in identical conditions, this was so that a post growth annealing study could be performed. The initially

Film Label	Substrate	Growth Pressure
PLD61_1	$SrTiO_3$	0.2 mTorr
PLD61_2	$SrTiO_3$	~4 mTorr
PLD61_3	$SrTiO_3$	80 mTorr
PLD61_4	$SrTiO_3$	0.2 mTorr
PLD62_1	sapphire	0.2 mTorr
PLD62_2	sapphire	~4 mTorr
PLD62_3	sapphire	80 mTorr
PLD62_4	sapphire	0.2 mTorr
PLD63_1	silicon	0.2 mTorr
PLD63_2	silicon	~4 mTorr
PLD63_3	silicon	80 mTorr
PLD63_4	silicon	0.2 mTorr
PLD65_1	glassy carbon	0.2 mTorr

Table 7.1: A summary of $SrFeO_{3-\delta}$ samples produced by PLD.

grown samples were 5 mm^2 in size and it was thought to be impractical to divide the substrates into three separate pieces for the annealing study, so a new batch of larger, 10 mm^2 substrates were prepared.

7.1.2 Post growth annealing

After deposition a selection of the films were chosen for further annealing. Two different annealing regimes were used, one to increase the oxygen content and another to decrease the oxygen content of the films. An (L) or (D) has been placed after the film label to easily identify the samples that have been oxygen loaded and oxygen depleted, respectively (table 7.2).

The samples were oxygen loaded by placing them in a crucible and then inserting them into a furnace. A steady flow of oxygen was passed through the

Film Label	Substrate	Growth Pressure	Annealing
PLD061_4	SrTiO3	0.2 mTorr	none
PLD061_4(L)	SrTiO3	0.2 mTorr	O-Loaded
PLD061_4(D)	SrTiO3	0.2 mTorr	O-Depleted
PLD062_3	sapphire	80 mTorr	none
PLD062_3 (D)	sapphire	80 mTorr	O-Depleted
PLD062_4	sapphire	0.2 mTorr	none
PLD062_4 (L)	sapphire	0.2 mTorr	O-Loaded
PLD065_1	glassy carbon	0.2 mTorr	none
PLD065_1(L)	glassy carbon	0.2 mTorr	O-Loaded
PLD065_1(D)	glassy carbon	0.2 mTorr	O-Depleted

Table 7.2: Annealing summary of $SrFeO_{3-\delta}$ samples.

furnace and the samples were heated to 600 ^{o}C. The samples remained at 600 ^{o}C in the oxygen rich environment for 5 hours, allowing the oxygen to be incorporated into the films. The samples were then cooled over a 6 hour period to 400 ^{o}C where they were left for a further 12 hours allowing the oxygen to diffuse into the film and create a uniform stoichiometry. The samples were then cooled to room temperature over a 12 hour period and removed from the furnace.

Oxygen depletion of the samples was performed in the same furnace using nitrogen in place of oxygen. The samples were heated to 500 ^{o}C, where they were left to diffuse for 5 hours. The samples were then rapidly cooled to 200 ^{o}C by pulling them away from the heat source of the furnace but still keeping them enclosed with a steady flow of nitrogen to prevent oxidisation. The samples were removed from the furnace once they had dropped below 200 ^{o}C.

All of the films were found to be transparent after deposition, with the samples grown at 80 mTorr being slightly darker in appearance than the films grown at 0.2 and 4 mTorr. After annealing, the optical properties of the films notable changed. Films that were annealed in nitrogen to deplete oxygen became more transparent and the films that were oxygen loaded became a metallic like colour (figure 7.1). $SrFeO_{3-\delta}$ is known to become metallic for oxygen concentration of $3-\delta = 2.875$ or greater, this indicates the as grown and depleted samples have oxygen concentrations less than 2.875, while the oxygen loaded sample has an oxygen content equal to or greater than the tetragonal, $SrFeO_{2.875}$.

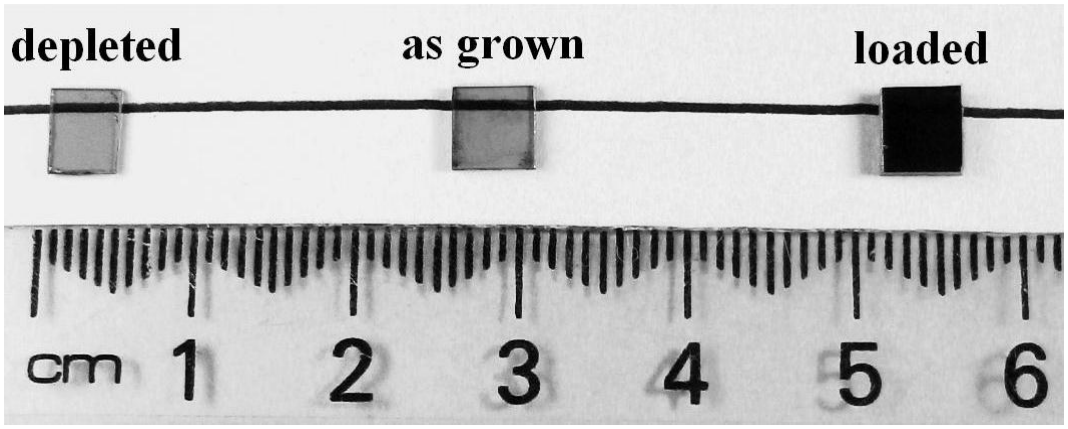

Figure 7.1: Photograph of three $SrFeO_{3-\delta}$ films deposited on double side polished sapphire substrates, showing the transparency of the films as grown, after annealing in nitrogen (depleted) and after annealing in oxygen (loaded). The samples have been placed on a piece of card with a black line drawn on it to illustrate their transparency.

7.2 Structural characterisation

7.2.1 Microscope images

High magnification images of the samples were taken using an Olympus BX60M microscope. The films deposited on $SrTiO_3$ and sapphire substrates were found to be smooth within the instruments limits, however, the problem of surface debris that was found on the Co:TiO_2 and SFMO samples was also present on the surface of the $SrFeO_{3-\delta}$ films. The films deposited on silicon had patches of smooth film but also showed large areas of extreme roughness and discolouration, indicating the surfaces of the silicon substrates were contaminated with some impurity prior to the deposition of the film (figure 7.2). The sample PLD63_3 was the only sample grown on silicon which was not affected in this way.

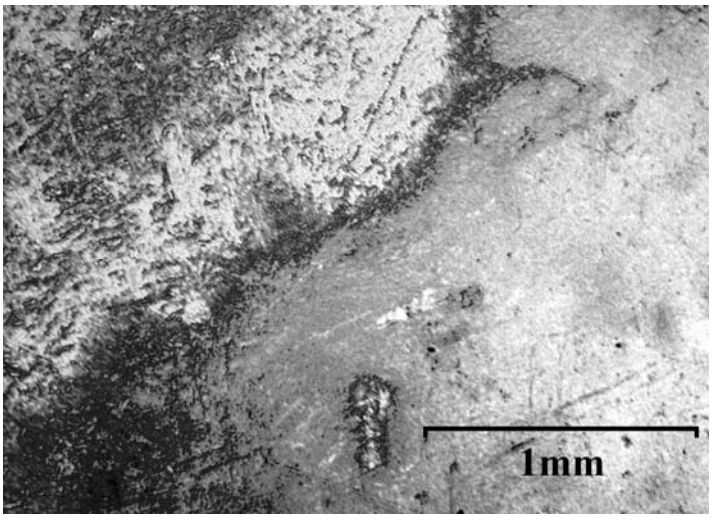

Figure 7.2: Microscope image of the silicon sample PLD63_2 taken at 5x magnification. The film deposited on the left of the image is very rough, indicating an impurity was present on the substrate surface prior to growth.

7.2.2 X-ray diffraction

X-ray diffraction measurements of the films grown in 0.2 and 4 mTorr of oxygen partial pressure showed little variation when compared. However, XRD data of the films grown at 80 mTorr was noticeably different, indicating a higher oxygen content in these films. The XRD data of the $SrTiO_3$ samples in combination with their transparent yellow colour, suggests the oxygen content of the films deposited in 0.2 and 4 mTorr of oxygen pressure is around $SrFeO_{2.75}$ and that the films have adopted the orthorhombic crystal structure. However, the films are highly strained by ~0.7^o which implies there may be more oxygen in the films than what is expected for the ideal orthorhombic structure.

The $SrTiO_3$ sample, PLD61_3 deposited in 80 mTorr of oxygen shows very different XRD data, suggesting that the crystal structure has changed to a value closer to the cubic, δ-3 = 3. The increase in oxygen was also evident in the non-transparent, metallic like colour of the film. The sample PLD61_4(L) which was oxygen loaded by annealing showed a similar XRD pattern to the sample grown in 80 mTorr of oxygen. When the samples are more closely compared we find that growing in a low oxygen pressure and then annealing creates a more oriented film that attempting to deposit at high oxygen pressures, as verified by XRD rocking curves. Annealing in nitrogen also had an affect on the XRD of the $SrTiO_3$ samples although it was much less pronounced, suggesting that only a small amount of oxygen was removed during depletion.

The sapphire samples showed XRD data similar to the $SrTiO_3$ samples with the as grown samples clearly showing the orthorhombic phase, which is attributed to δ-3 = 2.75. Unlike the $SrTiO_3$ sample, increasing the deposition pressure did not result in a metallic like film, although the sapphire sample deposited at 80 mTorr was less transparent than the films deposited in lower pressures. As with the $SrTiO_3$ samples the films were strained, indicating that more than the ideal amount of oxygen for the orthorhombic structure was present. Annealing in oxygen was again found to have a large effect on the structure and oxygen content of the films. The sample, PLD62_4(L), annealed in an oxygen gas shows a clear change in its structure from orthorhombic to cubic when compared with the as grown sample PLD62_4 (figure 7.3). The anneal in nitrogen, to deplete oxygen

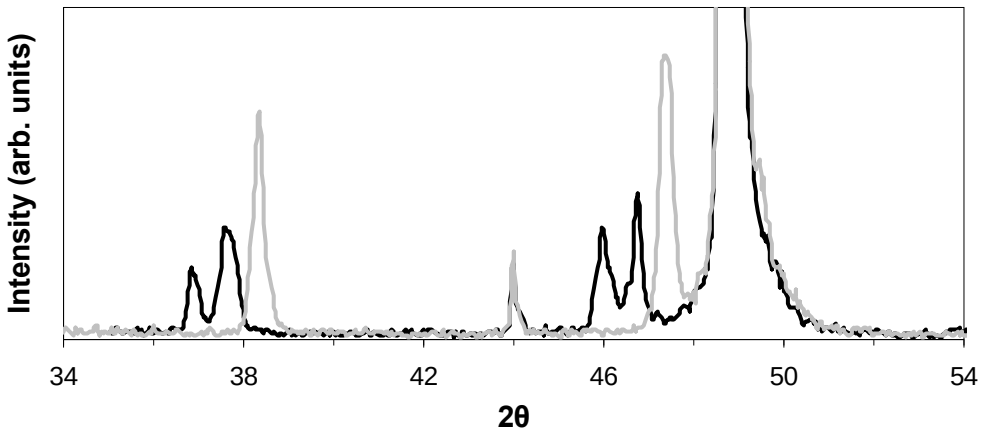

Figure 7.3: X-ray diffraction data for the two sapphire samples, PLD62_4 (black line) and PLD62_4(L) (grey line) showing a structural transition after the sample is loaded with oxygen by annealing. The peaks at 44.0^o and 48.8^o are the sapphire β and α peaks, respectively.

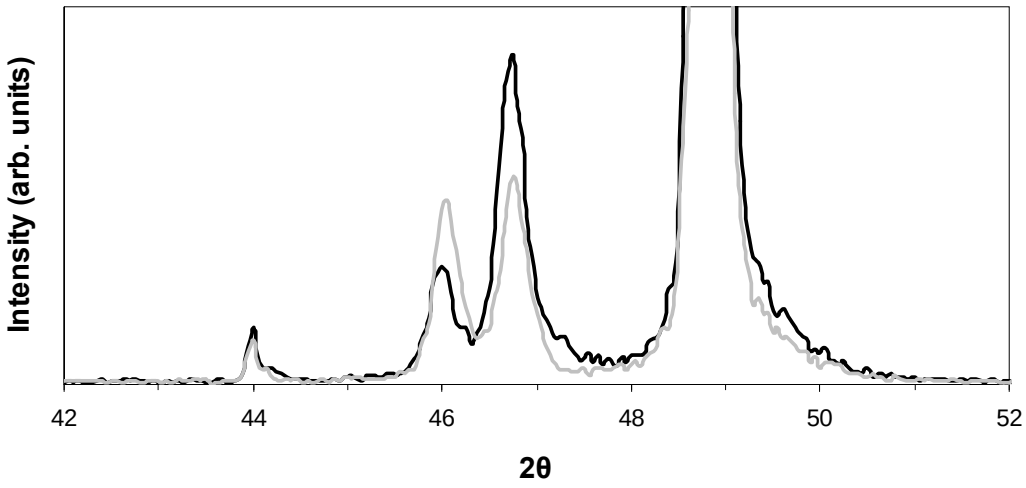

Figure 7.4: X-ray diffraction data for the two sapphire samples, PLD62_3 (black line) and PLD62_3(D) (grey line) showing a small structural transition after the sample is oxygen depleted by annealing. The peaks at 44.0^{o} and 48.8^{o} are the sapphire β and α peaks, respectively.

was found to have a less dramatic effect on the XRD data, with less change shown, indicating that depletion does not change the structure as significantly as the oxygen loading (figure 7.4).

7.2.3 Rutherford backscattering spectroscopy

Rutherford backscattering measurements of the samples were performed by Dr. John Kennedy. The thickness of the films was found to be 250 $^{+}$/- 20 nm. The two carbon samples, PLD65_1(D) (oxygen depleted) and PLD65_1 (as grown) were measured as the carbon substrates are amorphous and do not show any peaks in RBS data, allowing us to get a good indication of the oxygen content. The two films were found to have stoichiometries of $SrFeO_{2.9}$ and $SrFeO_{2.8}$ on the as

grown and oxygen depleted samples, respectively. However, from the XRD measurements of the samples we found that the as grown samples were close to $SrFeO_{2.75}$, in disagreement with the predictions made from the RBS data. We can be fairly confident in this initial prediction due to the transparent nature of the as grown films. If the oxygen content was near 2.9 then we would not expect films that are 250 nm thick to be non-transparent, as they would be close to the metallic like phase, $3-\delta = 2.875$. Due to the complexities of analysing RBS data it can be difficult to obtain accurate stiochiometries for the samples, and although the relative concentrations of oxygen in the samples is probably well estimated, the actual oxygen content of the samples may vary from the estimations. Hence from the combined XRD and RBS data we conclude the stoichiometry of the two samples are close to $SrFeO_{2.75}$ and $SrFeO_{2.65}$ for the as grown and oxygen depleted samples, respectively.

7.3 Magnetic response

The films were analysed with the SQUID magnetometer. However, because the samples were antiferromagnetic, their signal strength was too low to obtain any meaningful data. It is known that the oxygen content of the films can be extracted by comparing field cooled and zero field cooled measurements but due to the low signal, the difference in field cooled and zero field cooled measurements was negligible. A previous student at Industrial Research Limited., E. K. Hemery,

made bulk polycrystalline targets of $SrFeO_{3-\delta}$ and obtained magnetisations on the order of 30 000 A/m at 6 T [36]. If we consider the volume of our films then we would expect to see a magnetic moment of ~ 2×10^{-10} emu at 6 T. Unfortunately, this is two orders of magnitude below the sensitivity of the SQUID (~10^{-8} emu), which explains the lack of any meaningful magnetic data.

7.4 Summary

A combination of PLD and post growth annealing have been used to create $SrFeO_{3-\delta}$ films with oxygen phases ranging from $3-\delta \sim 2.65$ to values approaching the cubic phase, $3-\delta = 3$. The samples deposited in oxygen pressures of 4 mTorr or less were found to have adopted the orthorhombic phase, $SrFeO_{2.75}$. Films deposited on sapphire substrates at 80 mTorr were found to have increased in oxygen content but were still less than the metallic phase, $SrFeO_{2.875}$, while the films deposited in 80 mTorr on $SrTiO_3$ substrates were a metallic like colour indicating the oxygen content of the film was $SrFeO_{2,875}$ or greater. For both sapphire and $SrTiO_3$ samples we found that annealing in oxygen after depositing the film at low pressure, produced higher quality, oriented films when compared to increasing the oxygen pressure up to 80 mTorr during deposition.

Summary and conclusions

In this thesis, we deposited thin films of Co:TiO_2, Sr_2FeMoO_6 and $SrFeO_{3-\delta}$ by pulsed laser deposition. The effect of the growth parameters on the structural, optical, electric and magnetic properties of the resultant films was measured and analysed. Here we present the main conclusions of this thesis, as well as possible ways that this work may be extended and improved.

In Chapter 3, we showed the various instruments used to synthesise and characterise Co:TiO_2, Sr_2FeMoO_6 and $SrFeO_{3-\delta}$ thin films. We also showed the process' employed to create the targets that were used to deposit the films. We found a $CoTiO_3$ impurity phase in the initial Co:TiO_2 targets; this impurity was reduced by up to ~80 % by cooking the targets in a nitrogen gas rather than air. The Sr_2FeMoO_6 target was also found to show impurity phases after an initial cook in air, with both $SrMoO_4$ and $SrFeO_3$ present in the XRD. These impurities were removed by re-grinding the target and performing a succession of cooks in a N_2/H_2 gas. A dense $SrFeO_{3-\delta}$ target was created by three successive cooks in air at ~1200 ^oC, with the target being ground and repressed after each cook to ensure good homogeneity. The target was then oxygen loaded creating a target with an oxygen content around, $3-\delta = 2.95$.

In chapter 4, we studied the effect of oxygen pressure and substrate temperature during growth on the structural and optical properties of TiO_2 films.

Many of the films were found to be peeling off the substrates when viewed under the microscope. This was strange as film peeling is much more common in thick films, and these films were likely to be under 100 nm in thickness. All of the films grown on sapphire substrates were found to be single phase rutile in the (200) orientation, as confirmed by X-ray diffraction measurements. The rutile peak of the films was found to be shifted by 0.45^{o} to 0.65^{o} from the expected position. The shift was less for the films grown at higher temperatures, where the higher temperatures were thought to increase diffusion during growth, allowing for more lattice relaxation. Rocking curves of the rutile peak on these samples had FWHM's of ~0.1^{o}, showing the films were highly orientated. Scanning electron microscope images suggested that the grain size of the films could be controlled by varying the oxygen pressure during growth, with higher growth pressures resulting in the formation of larger grains. The optical band gaps calculated from the optical transmission data ranged from 2.9 to 3.3 eV.

In chapter 5, we expanded on our study of TiO_2 films by using TiO_2 targets doped with cobalt. We deposited thin films of Co:TiO_2 on sapphire, silicon and $SrTiO_3$ substrates and found that the substrate choice had a large effect on the resulting crystal structure of the films. The sapphire, silicon and $SrTiO_3$ substrates where found to favour the formation of, highly orientated (200) rutile, polycrystalline rutile and (004) anatase, respectively. The difference in the crystal phases formed was attributed to the close lattice matches between TiO_2 anatase and $SrTiO_3$ and the TiO_2 rutile phase and sapphire. While the polycrystalline

nature of the films on silicon substrates was explained by the large lattice mismatch between silicon and the TiO_2 crystal structures. No impurity phases were found on the sapphire or $SrTiO_3$ samples, although a small $CoTiO_3$ impurity peak was found in an XRD grazing incidence scan of one of the silicon samples. Transmission data showed the films to be optically transparent in the visible region with optical band gaps greater than 3 eV. To further understand the optical properties of the films future measurements of the reflectivity as well as transmission need to be taken and compared.

Ferromagnetic behaviour was observed in the films up to 300 K with a detailed study on one particular sapphire sample (PLD43_4) suggesting a Curie temperature of ~600 ^{o}C. The saturation moments of the films were found to be highly dependant on the substrate choice with the highest values up to 7.0 μ_B/Co being measured for films deposited on silicon and the lowest values down to 0.2 μ_B/Co being recorded for films deposited on $SrTiO_3$. We were unable to detect any ferromagnetic impurities in our samples or any evidence of cobalt clustering, leading us to believe the ferromagnetism observed in our samples was intrinsic. The oxidisation state of cobalt in Co:TiO_2 films has been determined to be 2+ by a number of researchers, but the local environment of cobalt in films exhibiting high values of m_s has not yet been studied. X-ray absorption spectroscopy of our films would of interest to see if the cobalt in our films is in the 3+ or 4+ state, which could help to understand the high moments observed in our films.

In chapter 6, we presented the results from the growth and characterisation of thin films of the double perovskite, Sr_2FeMoO_6. The films were deposited on silicon, sapphire and $SrTiO_3$ substrates, with RBS data showing the films to be approximately 450 nm thick. XRD data showed the films deposited on $SrTiO_3$ substrates had adopted the (004) orientation of SFMO and rocking curves of these peaks had FWHM's of ~0.3^o showing the films were highly orientated. The films deposited on sapphire and silicon substrates were found to be polycrystalline, with the exception of one oriented peak on the sapphire substrates that was attributed to (311) orientated SFMO. Peaks of the impurity phase, $SrMoO_4$ were found in some of the grazing incidence scans. It is believed that this impurity was responsible for the formation of microstructures, which were observed on some of the sample surfaces under an optical microscope. These impurity peaks were found to be more dominant on samples grown at higher temperatures suggesting the samples may have been decomposing.

The higher growth temperatures were also found to increase the magnetic saturation of the films, with the increase in growth temperature from 650 ^{o}C to 850 ^{o}C increasing the saturation moments of the films by over 200 %. Films deposited on silicon recorded the highest moments for all growth conditions, with the film deposited at 850 ^{o}C (PLD60_2) having a saturation moment of 2.8 μ_B/f.u. The substrate choice had a very quantifiable effect on the saturation moments of the films, with silicon giving the highest saturation moments and sapphire showing the lowest saturation moments for all growth conditions. Field loops

performed at 300 K on the films showed reductions in the saturation moments of 10 to 20 % when compared to 10 K measurements, consistent with Curie temperatures of around 450 ^{o}C, that are commonly reported in the literature. The observed MR of SFMO is one of its most interesting properties and future measurements of the resistance as a function of applied field for our films would be of great interest.

In chapter 7 we showed the results of a small growth study on the oxygen deficient $SrFeO_{3-\delta.}$ Thin films with oxygen phases ranging from just below the ideal orthorhombic phase, $3-\delta = 2.75$ to values approaching the cubic phase, $3-\delta = 3$ were deposited on $SrTiO_3$, sapphire and silicon substrates. It was found that annealing in an oxygen gas after growth was a better way of producing films with higher oxygen contents compared to increasing the oxygen pressure during PLD growth, where the increased growth pressure was found to reduce the crystalline quality of the films. The samples deposited in oxygen pressures of 4 mTorr or less were found to have adopted the orthorhombic phase, while the films that were deposited at 80 mTorr, or oxygen loaded, adopted the cubic structure indicating they had an oxygen contents close to, $3-\delta = 3$. Future measurements of the transport properties would be of interest to further characterise the unique properties of this compound in thin film form. We would also be interested in using better quality silicon substrates or improving our pre-growth cleaning of the substrates, so that quality $SrFeO_{3-\delta}$ films can be deposited onto silicon substrates in future growths.

References

[1] H. Akinaga, H. Ohno, IEEE Trans. Nanotech. **1**, 19 (2002).

[2] S.A. Chambers, T. Droubay, C.M. Wang, A.S. Lea, R.F.C. Farrow, L. Folks, V. Deline, S. Anders, Appl. Phys. Lett. **82**, 1257 (2003).

[3] J.Y. Kim, J.H. Park, B.G. Park, H.J. Noh, S.J. Oh, J.S. Yang, D.H. Kim, S.D. Bu, T.W. Noh, H.J. Lin, H.H. Hsieh, C.T. Chen, Phys. Rev. Lett. **90**, 017401 (2003).

[4] D.H. Kim, J.S. Yang, K.W. Lee, S.D. Bu, T.W. Noh, S.J. Oh, T.W. Kim, J.S. Chung, H. Tanaka, H.Y. Lee, T. Kawai, Appl. Phys. Lett. **81**, 2421 (2002).

[5] T. Manako, M. Izumi, Y. Konishi, K.I. Kobayashi, M. Kawasaki, Y. Tokura, Apll. Phys. Lett. **74**, 2215 (1999).

[6] Y. Tomioka, T. Okuda, Y. Okimoto, R. Kumai, K. I. Kobayashi, Y. Tokura, Phys. Rev. B **61**, 422 (2000).

[7] A. Lebon, P. Adler, C. Bernhard, A.V. Boris, A.V. Pimenov, A. Maljuk, C.T. Lin, C. Ulrich, B. Keimer, Phys. Rev. Lett. **92**, 037202-1 (2004).

[8] K. M. Yu, W. Walukiewicz, T. Wojtowicz, I. Kuryliszyn, X. Liu, Y. Sasaki, J. K. Furdyna, Phys. Rev. B **65**, 201303 (2002).

[9] S.A. Chambers, S. Thevuthasan, R.F.C. Farrow, R.F. Marks, J.U. Thiele, L. Folks, M.G. Samant, A.J. Kellock, N. Ruzycki, D.L. Ederer, U. Diebold, Appl. Phys. Lett. **79**, 3467 (2001).

[10] C.E. Rodriguez Torres, A.F. Cabera, L.A. Errico, S. Duhalda, M. Renteria, F. Golmar, F.H. Sanchez, Physica B **398**, 219 (2007).

[11] K.A. Griffen, A.B. Pakhomov, C.M. Wang, S.M. Heald, K.M. Krishnan, Phys. Rev. Lett. **94**, 157204 (2005).

[12] H.S. Yang, R. Singh, J. Appl. Phys. **97**, 043902 (2005).

[13] J.E. Jaffe, T.C. Droubay, S.A. Chambers, J. Appl. Phys. **97**, 073908 (2005).

[14] H.H. Nguyen, W. Prellier, J. Sakai, A. Ruyter, J. Appl. Phys. **95**, 7378 (2004).

[15] S.R. Shinde, S.B. Ogale, S. Das Sarma, J.R. Simpson, H.D. Drew, S.E. Lofland, C. Lanci, J.P. Buban, N.D. Browning, V.N. Kulkarni, J. Higgens, R.P. Sharma, R.L. Greene, T. Venkatesan, Phys. Rev. B **67**, 115211 (2003).

[16] R. Janisch, N. Spajdin, Phys. Rev. B **73**, 035201 (2006).

[17] A.K. Rumaiz, B. Ali, A. Ceylan, M. Boggs, T. Beebe, S. Ismat Shah, Solid State Comm. **144**, 334 (2007).

[18] C. Sudakar, P. Kharel, R. Suryanarayanan, J.S. Thakur, V.M. Naik, R. Naik, G. Lawes, J. Magn. Magn. Mater. **320**, L31 (2008).

[19] T. Fang, Phys. Rev. B **71**, 064401 (2005).

[20] M. Retuerto, J.A. Alonso, M.J. Martinez-Lope, J.L. Martinez, M. Garcia-Hernandez, Appl. Phys. Lett. **85**, 266 (2004).

[21] D. Sanchez, M. Garcia-Hernandez, N. Auth, G. Jakob, J. Appl. Phys. **96**, 2736 (2004).

[22] X.H. Li, Y.P. Sun, W.J. Lu, R. Ang, S.B. Zhang, X.B. Zhu, W.H. Song, J.M. Dai, Solid State Comm. **145**, 98 (2008).

[23] J. S. Kang, H. Han, B.W. Lee, C. G. Olson, S. W. Han, K. H. Kim, J. I. Jeong, J. H. Park, B. I. Min, Phys. Rev. B **64**, 024429 (2001).

[24] T. saitoh, M. Nakatake, A. Kakizaki, H. Nakajima, O. Morimoto, S. Xu, Y. Moritomo, N. Hamada, Y. Aiura, Phys. Rev. B **66**, 035112 (2002).

[25] E.K. Hemry, G.V.M. Williams, H.J. Trodahl, Phys. Rev. Lett. B **74**, 054423 (2006).

[26] D. D. Sarma, Curr. Opin. Solid state Meter. Phys. **5**, 261 (2001).

[27] E.K. Hemry, G.V.M. Williams, H.J. Trodahl, Current Appl. Phys. **6**, 312 (2006).

[28] H. Sakuma, T. Taniyama, Y. Kitamoto, Y. Yamazaki, J. Appl. Phys. **93**, 2816 (2002).

[29] E.K. Hemery, G.V.M. Williams, H.J. Trodahl, The effect of isoelectric substitution on the magnetoresistance of SrBaFeMoO, Physica B (2006).

[30] J. B. Goodenough, Phys. Rev. B **100**, 564 (1955).

[31] T. Takeda, Y. Yamaguchi, H. Wantanabe, J. Phys. Soc. Jpn. **33**, 967 (1972).

[32] J.P. Hodges, S. Short, J.D. Jorgensen, X. Xiong, B. Dabrowski, S.M. Mini, C.W. Kimball, J. Solid State Chem. **151**, 190 (2000).

[33] P. K. Gallagher, J. B. MacChesney, D. N. E. Buchanan, J. Chem. Phys. **41**, 2429 (1964).

[34] P. Adler, A. Lebon, V. Damljanovic, C. Ulrich, C. Bernhard, A. V. Boris, A. Maljuk, C. T. Lin, B. Keimer, Phys. Rev. B **73**, 094451 (2004).

[35] A. Lebon, P. Adler, B. Bernhard, A. V. Boris, A. V. Pimenov, A. Maljuk, C. T. Lin, C. Ulrich, B. Keimer, Phys. Rev. Lett. **92**, 037202 (2004).

[36] G. V. M. Williams, E. K. Hemery, D. McCann, Phys. Rev. B **79**, 024412 (2009).

[37] J. Kim, S. Lee, H. Im, Appl. Surf. Sci. **151**, 6 (1999).

[38] E. K. Hemry, G. V. M. Williams, H. Trodahl, Curr. Appl. Phys. **6**, 312 (2006).

[39] N. Sbai, J. Perriere, W. Seiler, E. Millon, Surf. Sci. **601**, 5649 (2007).

[40] D. G. Syarif, A. Miyashita, T. Yamaki, T. Sumita, Y. Choi, H. Itoh, Appl. Surf. Sci. **193**, 287 (2002).

[41] S. Murugesan, P. Kuppusami, N. Parvathavarthini, E. Mohandas, Surf. Coating Tech. **201**, 7713 (2007).

[42] Z. Lei, L. Jian-she, Trans. Nonferrous Met. Soc. China **17**, 772 (2007).

[43] C. C. Hsieh, K. H. Wu, J. Y. Juang, T. M. Uen, J. Y. Lin, Y. S. Gou, J. Appl. Phys. **92**, 2518 (2002).

[44] S. Kitazawa, Y. Choi, S. Yamamoto, T. Yamaki, Thin Solid Films **515**, 1901 (2006).

[45] S. Yamamoto, T. Sumita, Sugiharuto, A. Miyashita, H. Naramoto, Thin solid Films **401**, 88 (2001).

[46] N. Martin, C. Rousselot, D. Rondot, F. Palmino, R. Mercier, Thin Solid Films **300**, 113 (1997).

[47] T. Tang, K. Prasad, R. Sanjines, P.E. Schmid, F. Levy, J. Appl. Phys. **75**, 2042 (1994).

[48] Y. D. Kim, S. L. Cooper, M. V. Klien, B. T. Jonker, Phys. Rev. B **49**, 1732 (1994).

[49] Y. D. Kim, S. L. Cooper, M. V. Klien, J. H. Park, B. T. Jonker, Phys. Rev. B **50**, 10637 (1994).

[50] M. J. Calderón and S. Das Sarma, Annals of Phys. **322**, 2618 (2007).

[51] T. Fukumura, H. Toyosaki, K. Ueno, M. Nakano, and M. Kawasaki, New J. Phys. **10**, 055018 (2008).

[52] R. Ramaneti, J. C. Lodder, and R. Jansen, Phys. Rev. B **76**, 195207 (2007).

[53] T. Hitosugi, G. Kinoda, Y. Yamamoto, Y. Furubayashi, K. Inaba, Y. Hirose, K. Nakajima, T. Chikyow, T. Shimada, T. Hasegawa, J. Appl. Phys. **99**, 08M121 (2006).

[54] R. Janisch, P. Gopal, N. A. Spaldin, J. Phys.: Condens. Matter **17**, 657 (2005).

[55] R. Suryanarayanan, V.M. Naik, P. Kharel, P. Talagala. R. Naik, Solid State Comm. **133**, 439 (2005).

[56] T. C. Kaspar, T. Droubay, C. M. Wang, S. M. Heald, A. S. Lea, S. A. Chambers, J. Appl. Phys. **97**, 073511 (2005).

[57] N. H. Hong, J. Sakai, W. Prellier, A. Hassini, A. Ruyter, F. Gervais, Phys. Rev. B **70**, 195204 (2004).

[58] M. Venkatesan, C. B. Fitzgerald, J.G. Lunney, and J.M. D. Coey, Phys. Rev. Lett. **93**, 177206 (2004).

[59] A. S. Risbud, N. A. Spaldin, Z. Q. Chen, S. Stemmer, R. Seshadri, Phys. Rev. B **68**, 205202 (2003).

[60] CRC handbook of chemistry and Physics, 84th ed. Edited by D. R. Lide (CRC, Boca Raton, FL, 2003).

[61] Y. Xin, K. Han, P.A. Stampe, R.j. Kennedy, J. Cry. Growth **290**, 459 (2006).

[62] S.R. Shinde, S.B. Ogale, R.L. Greene, T. Venkatesan, K. Tsoi, S.W. Cheong, A.J. Millis, J. Appl. Phys. **93**, 1605 (2002).

[63] T. Fix, G. Versini, J.L. Loison, S. Colis, G. Schmerber, G. Pourroy, A. Dinia, J. Appl. Phys. **97**, 024907, (2005).

[64] J. Santiso, A. Figueras, J. Fraxedas, Surf. Interface Anal. **33**, 676 (2002).

[65] J.H. Song, J. H. Park, Y. H. Jeong, J. Appl. Phys. **97**, 046105 (2005).

[66] A. Venimadhav, F. Sher, J.P. Attfield, M.G. Blamire, J. Magn. Magn. Mater. **269**, 101 (2004).

[67] I.R. Shein, V.L. Kozhevnikov, A.L. Ivanovskii, J. Phys. Chem. Solids **67**, 1436 (2006).

[68] E.K. Hemry, G.V.M. Williams, H.J. Trodahl, Phys. Rev. B **75**, 092403 (2007).

[69] Optical properties of condensed matter and applications, edited by Jai Singh (Wiley, 2006)